Testing the Black Hole No-hair Theorem with Galactic Center Stellar Orbits

Hong Qi,[1,2,*] Richard O'Shaughnessy,[3] and Patrick Brady[2]

[1] *School of Physics and Astronomy, Cardiff University, Cardiff CF24 3AA, United Kingdom*
[2] *Center for Gravitation Cosmology and Astrophysics, University of Wisconsin-Milwaukee, Milwaukee, WI 53201, USA*
[3] *Center for Computational Relativity and Gravitation, Rochester Institute of Technology, Rochester, NY 14623, USA*

(Dated: November 5, 2020)

Theoretical investigations have provided proof-of-principle calculations suggesting measurements of stellar or pulsar orbits near the Galactic Center could strongly constrain the properties of the Galactic Center black hole, local matter, and even the theory of gravity itself. As in previous studies, we use a Markov chain Monte Carlo to quantify what properties of the Galactic Center environment measurements can constrain. In this work, however, we also develop an analytic model (Fisher matrix) to understand what parameters are well-constrained and why. Using both tools, we conclude that existing astrometric measurements cannot constrain the spin of the Galactic Center black hole. Extrapolating to the precision and cadence of future experiments, we anticipate that the black hole spin can be measured with the known star S2. Our calculations show that we can measure the dimensionless black hole spin to an accuracy and a precision of $\sim$0.1 with weekly measurements of the orbit of S2 for 40 years using the GRAVITY telescope's best resolution at the Galactic Center, i.e., an angular resolution of 10 micro-arcsecond and a radial velocity resolution of 500 m/s. We derive an analytic expression for the measurement uncertainty of the black hole spin using Fisher matrix in terms of observation strategy, star's orbital parameters, and instrument resolution. We conclude that highly eccentric orbit can provide better constraints on the spin, and an orbit with a higher eccentricity is more favorable even when the orbital period is longer. Besides, if we can find N stars that have similar orbits to S2, we can reduce the observation time by a factor of $\sqrt{N}$ while remaining the same measurement uncertainty of the black hole spin. If in addition future measurements include discovery of a new, tighter stellar orbit, then future data could conceivably enable tests of strong field gravity, by directly measuring the black hole quadrupole moment. Our simulations show that with a stellar orbit similar to that of S2 but at one fifth the distance to the Galactic Center and GRAVITY's resolution limits on the Galactic Center, we can start to test the no-hair theorem with 20 years of weekly orbital measurements.

I. INTRODUCTION

The supermassive black hole at the center of our galaxy provides unique opportunities to investigate dynamics near a strongly-gravitating source [1, 2]. Radio telescopes have imaged the immediate vicinity of the black hole [3, 4], allowing direct constraints on the strong gravitational field regime near the black hole via imaging accretion flows [5–9]. Stellar motions also constrain the number and orbits of nearby perturbers [10]. At present, however, the best opportunities to constrain the Galactic Center come from long-term monitoring of known stars [11–15]. These measurements can also identify effects from the strong gravitational field [16–18] and the properties of the supermassive black hole [2, 11–13, 19–24]. Even stronger constraints would be possible with a well-timed pulsar orbiting the Galactic Center [25–29], at separations comparable to a recently-discovered object [30]. High precision inference from stellar orbits ideally should account for many nearby perturbers, including the local stellar density of visible stars [31] and compact objects [21].

Motivated by recent discoveries of new stars in close orbits around the galactic center [32, 33], we assess how well existing and future measurements of stellar orbits [2] can constrain the black hole properties: its mass and particularly its spin. Specifically, we wrote a Markov chain Monte Carlo (MCMC) code and use it to compare real and synthetic astrometric and radial velocity data with models for the stellar orbits and black hole mass, accounting for differences in reference frame between different observational campaigns. Unlike previous investigations, our model includes leading order post Newtonian corrections to the orbit from the black hole's mass, spin, and quadrupole moment, as well as the impact of unknown non-quadrupole internal and exterior potentials. Our goal is to determine whether, despite the extremely low orbital velocity $v/c \simeq 0.02$, future measurements can significantly constrain strong-field features of the Galactic Center black hole. We compare our MCMC results against a detailed Fisher matrix analysis, both to validate our results and allow the reader to easily extrapolate to future measurement scenarios.

This paper is organized as follows. In Section II we review the observations of stellar orbits near the Galactic Center; review a simplified model for stellar dynamics near supermassive black holes (justified at length in Appendix A); introduce simplified and realistic models for the process of measuring stellar orbits, including errors. In Section III we describe two techniques to assess how well measurements can constrain properties of stellar orbits and the supermassive black hole. The first is a

* hong.qi@ligo.org

simplified, approximate Fisher matrix.

The second method uses detailed Markov chain Monte Carlo simulations of synthetic data to determine how well different parameters can be measured and why. After validating our procedure using analytically tractable toy models with a handful of parameters, we perform full-scale simulations in Section IV to test several hypotheses including no-hair theorem. Using plausible choices of parameters and future achievable measurement accuracy, we discuss how the black hole spin and quadrupole moment can be constrained with the known star S2 of an orbital period of about 16 years and future discoverable closer stars with orbital periods as small as 1-2 years [34]. In Section V we summarize the conclusions we draw from the studies. Throughout the paper we adopt the units where $G = c = 1$.

II. STATEMENT OF THE PROBLEM

A. Existing Observations

There are observations of stellar orbits within 1 arcsecond of the Galactic Center in infrared [12, 13, 15, 32]. In this paper, we are analyzing two sets of long-duration observations reported in Ghez et al. [12] and Gillessen et al. [13]. The motions of stars in the immediate vicinity of Sgr A* have been observed in infrared bands by NTT/VLT since 1992 and by Keck telescope since 1995. The two data sets we use are the Keck data from 1995 to 2007 and the VLT data from 1992 to 2009. Massive young stars are found closely orbiting the black hole at the center of our Milky Way. The locations of the stars, i.e., the astrometric positions, right ascensions (RA) and declinations (DEC) are recorded at different epochs. Therefore, the relative positions of stars to the radio source Sgr A*, i.e., the offsets of RA and DEC are also measured. The radial velocities, i.e., the line of sight components of the velocities relative the the observers, of each star at different epochs are also measured. In this work, we use the stellar orbits of star S2, because it is monitored for the longest time, its orbit is only 16 years which is the second shortest stellar orbital period known, and more importantly its eccentricity is the highest among the few closest orbits. The high eccentricity makes the star get deeper in the gravitational potential of the black hole and thus can provide more physics. We show in IV B with concrete simulations why the orbit of S2 provides better constraints than that of S102/S55 even though the latter has a smaller orbital period (12 years) even if they are observed the same way. There have been more recent observations and measurements of the S2 stellar orbit [35–37] as we prepared our paper, but the added data does not affect our conclusions.

B. Simplified models of stellar orbits

The approximations involved in deriving and justifying our equations of motion are provided in Appendix A. Neglecting the black hole's recoil or the effect of ambient material, each star's position $\mathbf{x}$ evolves according to leading-order post-Newtonian equations of motion [20, 38, 39]

$$\begin{aligned}\mathbf{a} = &-\frac{M\mathbf{x}}{r^3} + \frac{M\mathbf{x}}{r^3}(4\frac{M}{r} - v^2) + 4\frac{M\dot{r}}{r^2}\mathbf{v} \\ &-\frac{2J}{r^3}[2\mathbf{v}\times\hat{\mathbf{J}} - 3\dot{r}\hat{\mathbf{n}}\times\hat{\mathbf{J}} - 3\hat{\mathbf{n}}(\mathbf{L}\cdot\hat{\mathbf{J}})/r] \\ &+\frac{3}{2}\frac{Q_2}{r^4}[5\hat{\mathbf{n}}(\hat{\mathbf{n}}\cdot\hat{\mathbf{J}})^2 - 2(\hat{\mathbf{n}}\cdot\hat{\mathbf{J}})\hat{\mathbf{J}} - \hat{\mathbf{n}}], \end{aligned} \tag{1}$$

where $\mathbf{x}, \mathbf{v} = \partial_t\mathbf{x}, \mathbf{a} = \partial_t^2\mathbf{x}$ are the (harmonic) coordinate position, velocity, and acceleration of the star; where $r = |\mathbf{x}|$ is the coordinate distance of the star from the black hole; where $\hat{\mathbf{n}} = \mathbf{x}/r$ is a unit vector pointing towards the star; where $\mathbf{L} = \mathbf{x}\times\mathbf{v}$ is the orbital angular momentum; where $M, \mathbf{J}, Q_2 = -J^2/M$ are the mass, spin angular momentum, and quadrupole moment of the black hole; and where the hat over a quantity denotes its unit vector, such as $\hat{\mathbf{J}} = \mathbf{J}/J$. Each star evolves according to a post-Newtonian Hamiltonian in [40].

For the proof-of-concept analytic calculations, we separate timescales by *orbit-averaging* rather than work with the full Hamiltonian, following standard practice in celestial mechanics. For analytic simplicity, we will furthermore treat all perturbations at leading order, therefore performing an orbit average using a Newtonian orbit; for example, at leading order an equatorial orbit has the form $r(t) = p/(1 + e\cos\Phi(t))$, where $p = a(1-e^2)$ is a semilatus rectum, a is the semimajor axis, e is the eccentricity of the orbit, and $\Phi(t)$ is the orbital phase in terms of time t. Using standard methods of celestial mechanics [20, 41], we find the secular equations of motion for the orbit average ($\langle X\rangle$) of each star's Newtonian orbital angular momentum $\mathbf{L}_N \equiv \mu\mathbf{x}\times\mathbf{v}$ and Newtonian Runge-Lenz vector $\mathbf{A}_N \equiv \mu^2[\mathbf{v}\times(\mathbf{x}\times\mathbf{v}) - GM\hat{\mathbf{n}}]$:

$$\partial_t\langle\mathbf{L}_N\rangle = \vec{\Omega}\times\langle\mathbf{L}_N\rangle \tag{2}$$

$$\partial_t\langle\mathbf{A}_N\rangle = \vec{\Omega}\times\langle\mathbf{A}_N\rangle \tag{3}$$

$$\vec{\Omega} = \vec{\Omega}_S + \vec{\Omega}_J + \vec{\Omega}_Q \tag{4}$$

$$\vec{\Omega}_S = \hat{\mathbf{L}}_N\frac{A_S}{P} = \hat{\mathbf{L}}_N\frac{3}{p(a/M)^{\frac{3}{2}}} \tag{5}$$

$$\vec{\Omega}_J = [\hat{\mathbf{J}} - 3\hat{\mathbf{L}}(\hat{\mathbf{L}}\cdot\hat{\mathbf{J}})]\frac{A_J}{P} = [\hat{\mathbf{J}} - 3\hat{\mathbf{L}}(\hat{\mathbf{L}}\cdot\hat{\mathbf{J}})]\frac{2J/M}{(Mp^3)^{\frac{1}{2}}(\frac{a}{M})^{\frac{3}{2}}} \tag{6}$$

$$\vec{\Omega}_Q = -(\hat{\mathbf{J}}(\hat{\mathbf{J}}\cdot\hat{\mathbf{L}}) + \frac{1}{2}\hat{\mathbf{L}}(1 - 3(\hat{\mathbf{L}}\cdot\hat{\mathbf{J}})^2)\frac{A_Q}{P} \tag{7}$$

$$A_Q = \frac{3}{2}\frac{Q_2}{p^2(a/M)^{3/2}}, \tag{8}$$

where the expressions $\vec{\Omega}, \vec{\Omega}_S, \vec{\Omega}_J, \vec{\Omega}_Q$ are the orbital precession, P is the orbital period, the expressions A_S, A_J,

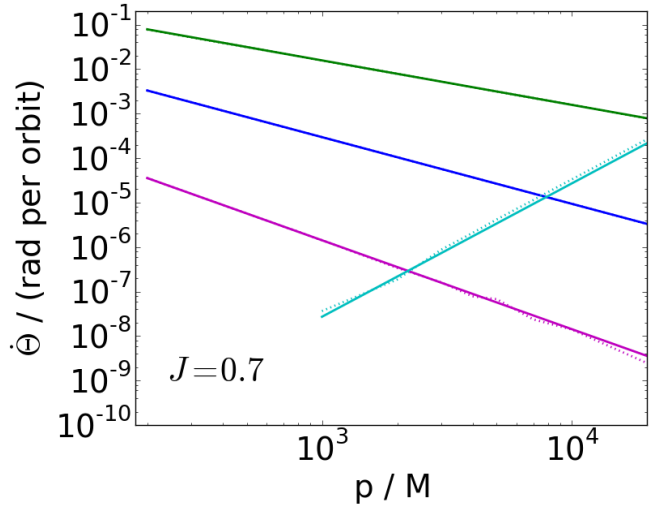

FIG. 1. Relative magnitude of characteristic rates of change for stellar orbits around supermassive black holes versus semi-latus rectum due to different effects. Solid curves show analytic results; dotted curves were derived from our time-domain evolution code, as validations. The solid green, blue, an purple curves show A_S, A_J, A_Q that are derived in [20] and implicitly defined in Eqs. (5), (6) and (7). The cyan curves show the influence of an external quadrupolar potential from ambient stars at a distance of 3×10^4 times the black hole mass.

A_Q were derived in [20] and are implicitly defined here; see also [42]. The factors A_S, A_J, and A_Q are shown in Figure 1. These orbit-averaged precession equations imply a straightforward procedure for the (linear) perturbation due to Ω, starting from a Newtonian solution $\vec{r}_o(t)$:

$$\vec{r}(t) \simeq R(t)\vec{r}_o(t), \tag{9}$$

where $R(t)$ is the rotation generated by the (orbit-averaged) $\vec{\Omega}$. Specifically, again working to first order in the orbit-averaged perturbations, the secular rotation $R(t)$ on short timescales is determined by the generators $\mathcal{L}_\alpha$ of rotations:

$$R(t) \simeq \mathbf{1} - it\mathcal{L}_\alpha\Omega^\alpha \tag{10}$$
$$\vec{r}(t) \simeq r_o(t) - it\Omega^\alpha\mathcal{L}_\alpha r_o(t). \tag{11}$$

C. Relationship between real observation and theoretical model

In order to use real data to measure the parameters of the whole system, we have to convert the measurements in the theoretical model in the Cartesian coordinates that originated at the black hole center to the real observed data form, RA and DEC offsets that are relative to Sgr A* in the Equatorial coordinate system which is centered at the Earth.

We first generate the orbit of a star with our mixed Python/Fortran code, and get the star's orbital positions, $\vec{r}_i^{bh} = \{x_i^{bh}, y_i^{bh}, z_i^{bh}\}$, in the black hole frame. Then we transformed from a Cartesian coordinates that centered at Sgr A* to the Equatorial RA and Dec, or in terms of components

$$x_i = x_i^{bh} + d\cos\alpha_{bh}\sin\delta_{bh} \tag{12}$$
$$y_i = y_i^{bh} + d\sin\alpha_{bh}\sin\delta_{bh} \tag{13}$$
$$z_i = z_i^{bh} + d\cos\delta_{bh}, \tag{14}$$

where d is the distance from the Earth to the center of black hole, α_{bh} and δ_{bh} are the RA and DEC of the black hole, x axis points to the First Point of Aries, and z axis points to the same direction as that in the black hole coordinates. The black hole Cartesian coordinates and the Earth Cartesian coordinates are only a translation of their origins described by $\vec{d}$. Then we convert the positions of the star from the Cartesian coordinate system that centers at the Earth to the Equatorial coordinate system,

$$\alpha_i = \arctan2(y_i, x_i) \tag{15}$$
$$\delta_i = \sin^{-1}\frac{z_i}{\sqrt{x_i^2 + y_i^2 + z_i^2}}, \tag{16}$$

where α_i is zero in the x-axis direction, and increases to 2π along the celestial equator counterclockwise as viewed from the North pole, and δ_i is zero in the celestial equator, positive to the north and negative to the south of the celestial equator. We subtract from $\{\alpha_i, \delta_i\}$ a reference position such as the astrometry position of Sgr A*, $\{\alpha_0 = 17\text{H } 43\text{M } 02\text{S} = 4.6383, \delta_0 = -28.7944°\}$ [43], and get the observed RA and DEC offsets relative to Sgr A*, $\{\Delta\alpha_i, \Delta\delta_i\}$, that are similar to those in the real data, where $\Delta\alpha_i = \alpha_i - \alpha_0$ and $\Delta\delta_i = \delta_i - \delta_0$. Note that the values of $\{\alpha_0, \delta_0\}$ for which we used in this paper have been fine-tuned over the years [44], but those values do not affect our study results because the observables are relative sky locations to $\{\alpha_0, \delta_0\}$, not absolute positions. As long as the measurements are always relative to the same object, it does not even matter whether we take Sgr A* as the reference. Notice the position of Sgr A* does not necessarily co-locate the center of the black hole. The difference between them can be modeled as five parameters, including the relative position of the black hole to the Sgr A*, $\Delta\alpha_{bh}$ and $\Delta\delta_{bh}$, and the uniform RA and DEC velocities and radial velocity, $\{v_{\alpha_{bh}}, v_{\delta_{bh}}, v_{r,bh}\}$, of the black hole relative to the Sgr A*. The radial velocities of the stellar orbit are evaluated as $v_{r,i} = \vec{v}_i \cdot \hat{r}_i$, where $\hat{r}_i = \vec{r}_i/r_i$ are the unit vectors of line of sight.

Based on our model, the following parameters are measured from the data: the six orbital parameters of the star $\{a, e, \Phi_0, \beta, \gamma, \psi\}$ (where a is semimajor axis, e is eccentricity, Φ_0 is the initial orbital phase at some moment, and the other three are Euler angles following a z-x-z definition), the three black hole spin components $\mathbf{J} = \{J_x, J_y, J_z\}$ in Cartesian coordinates or

$\mathbf{J} = \{J, \phi_J, \theta_J\}$ in Spherical coordinates as what we used in the code, the mass of the black hole M, the position of the black hole relative to the Sgr A* $\{d, \Delta\alpha_{bh}, \Delta\delta_{bh}\}$ (where d is the distance from Sgr A* to us and the other two indicate the black hole's astronomical position). We ignore the motion of the black hole relative to the Sgr A* $\{v_{\alpha_{bh}}, v_{\delta_{bh}}, v_{r,bh}\}$. To test the no-hair theorem, we also use two more parameters, the quadrupole term, Q_2, of black hole potential, and the quadrupole term, Q_X, due to the external potential of star clusters that extend between $40,000M$ and $80,000M$ to Sgr A*. Those two parameters can be combined into one parameter, the quadrupole term Q, where $Q = Q_2 + Q_X$. Throughout the paper everything is in the units of $M_* = 4.00\times10^6 M_\odot$ when we perform calculations.

III. MEASURING PARAMETERS

A. Bayesian formalism

According to the Bayesian paradigm, a prior distribution $p(\vec{\lambda})$ is used to quantify our knowledge about a set of unobservable parameters $\vec{\lambda}$ in a statistical model when no data are available. We can update our prior knowledge using the conditional distribution of parameters, given observed data, via the Bayes theorem. Suppose that the likelihood, or the distribution of the data from an assumed model that depends on the parameter $\vec{\lambda}$ is denoted by $p(D|\vec{\lambda})$, Bayes theorem updates the prior to the posterior by accounting for the data,

$$p(\vec{\lambda}|D) = \frac{p(D|\vec{\lambda})p(\vec{\lambda})}{p(D)}, \tag{17}$$

where $p(D) = \int p(D|\vec{\lambda})p(\vec{\lambda})d\vec{\lambda}$ is the evidence of the data and also a normalizing constant.

To separate issues pertaining to measurements from physics from simplified models of stellar orbits, we describe results using the real measurement scenario, where only the angular offsets and radial velocity can be measured. [For comparison and to validate our MCMC method, we also employ idealized theoretical measurement scenarios in Appendix C.] This realistic measurement model accounts for all of the parameters described in Section II C. The probability distribution of the data given parameters $\vec{\lambda}$ is

$$\begin{aligned} p(D|\vec{\lambda}) = &\prod_k^{N_{\Delta\alpha}} (2\pi\sigma^2_{\Delta\alpha_k})^{-1/2} \exp - \frac{[\Delta\alpha(t_k|\vec{\lambda}) - \Delta\alpha_k]^2}{2\sigma^2_{\Delta\alpha_k}} \\ &\times \prod_k^{N_{\Delta\delta}} (2\pi\sigma^2_{\Delta\delta_k})^{-1/2} \exp - \frac{[\Delta\delta(t_k|\vec{\lambda}) - \Delta\delta_k]^2}{2\sigma^2_{\Delta\delta_k}} \\ &\times \prod_k^{N_{v_r}} (2\pi\sigma^2_{v_{r,k}})^{-1/2} \exp - \frac{[v_r(t_k|\vec{\lambda}) - v_{r,k}]^2}{2\sigma^2_{v_{r,k}}}, \end{aligned} \tag{18}$$

where $\Delta\alpha(t_k|\vec{\lambda})$ and $\Delta\alpha_k$ are the theoretical prediction of the RA offset and the real observation, respectively, at epoch t_k; the notations are similar for the other two observables, i.e., DEC offset and radial velocity; $\sigma_{\Delta\alpha_k}$, $\sigma_{\Delta\delta_k}$, and $\sigma_{v_{r,k}}$ are measurement uncertainties for the observation at t_k. The number of measurements for the three observables are denoted as $N_{\Delta\alpha}, N_{\Delta\delta}, N_{v_r}$, respectively. In the equation above, we have assumed that each measurement of each observable has a noise of Gaussian distribution.

In order to determine the best-fit parameters and their uncertainties we use a Markov chain Monte Carlo analysis to sample the likelihood function in Eq. (18). Specifically, we use an ensemble sampler for MCMC named EMCEE [45, 46].

B. Fisher matrix

To better understand and validate our MCMC results, and to make efficient projections about future hypothetical measurements, we perform a semi analytic calculation that approximates the likelihood in Eq. (18) by a locally quadratic approximation. The coefficient of the second-order term is known as the Fisher matrix.

The illustration of the mechanics of a Fisher matrix calculation is shown in Appendix C by employing the idealized measurement model in Cartesian coordinates. For real observations, we can do the same by exploiting in the special case that the observed data is exactly as predicted by some set of model parameters $\vec{\lambda}'$ [i.e., $\Delta\alpha_k = \Delta\alpha(t_k|\vec{\lambda}')$, $\Delta\delta_k = \Delta\delta(t_k|\vec{\lambda}')$, and $v_{r,k} = v_r(t_k|\vec{\lambda}')$]. Using a first-order Taylor series expansion $\Delta\alpha(t_k|\vec{\lambda}) - \Delta\alpha(t_k|\lambda') \simeq \delta\lambda^a \partial\Delta\alpha(t_k)/\partial\lambda_a$ for the RA offset $\Delta\alpha$ versus parameters $\vec{\lambda}$ (here λ^a are the elements of $\vec{\lambda}$ and same index a means contraction) and similar for the other two observables, we find that the conditional probability of the data given $\vec{\lambda}$ can be approximated by

$$\ln p(D|\vec{\lambda}) = \text{const} - \frac{1}{2}\Gamma_{ab}\delta\lambda_a\delta\lambda_b \tag{19}$$

with

$$\Gamma_{ab} = \sum_k \left[\frac{C_{\lambda_a,\Delta\alpha_k} C_{\lambda_b,\Delta\alpha_k}}{\sigma^2_{\Delta\alpha_k}} + \frac{C_{\lambda_a,\Delta\delta_k} C_{\lambda_b,\Delta\delta_k}}{\sigma^2_{\Delta\delta_k}} + \frac{C_{\lambda_a,v_{r,k}} C_{\lambda_b,v_{r,k}}}{\sigma^2_{v_{r,k}}} \right], \tag{20}$$

where Γ_{ab} is the Fisher matrix. For a parameter in $\vec{\lambda}$ that has two values λ_a and λ'_a, with $\delta\lambda_a$ difference that results in two orbits, the components in Eq. (20) for this parameter are

$$C_{\lambda_a,\Delta\alpha_k} \equiv \frac{\partial \Delta\alpha(t_k)}{\partial \lambda_a} = \frac{\Delta\alpha(t_k|\lambda_a) - \Delta\alpha(t_k|\lambda'_a)}{\delta\lambda_a} \tag{21}$$

$$C_{\lambda_a,\Delta\delta_k} \equiv \frac{\partial \Delta\delta(t_k)}{\partial \lambda_a} = \frac{\Delta\delta(t_k|\lambda_a) - \Delta\delta(t_k|\lambda'_a)}{\delta\lambda_a} \tag{22}$$

$$C_{\lambda_a,v_{r,k}} \equiv \frac{\partial v_r(t_k)}{\partial \lambda_a} = \frac{v_r(t_k|\lambda_a) - v_r(t_k|\lambda'_a)}{\delta\lambda_a}. \tag{23}$$

Having estimated the Fisher matrix and hence approximated $p(D|\vec{\lambda})$ by a Gaussian, we can further construct marginalized distributions for subset variables λ_A in $\vec{\lambda} = (\lambda_A, \lambda_a)$ by integrating out the variables λ_a. In the gaussian limit, this integration implies the marginalized distribution has a covariance matrix $\bar{\Gamma}_{AB}$ given by

$$\bar{\Gamma}_{AB} = \Gamma_{AB} - \Gamma_{Aa}[\Gamma^{-1}]_{ab}\Gamma_{bB}. \tag{24}$$

Because the second term is negative, the marginalized distribution is always wider: adding additional uncertain degrees of freedom leads to less accurate measurements.

The Fisher matrix is a cross check for the parameter estimations obtained from MCMC. Drawing in the best-fit parameters, the Fisher matrix can give the estimates of the uncertainties of parameters in a few seconds, whereas it takes MCMC several hours in our problem. A Fisher matrix can also let us test how sensitively the measurement accuracy and hypothesis tests depend on stellar parameters. As an illustration of the usefulness of the Fisher matrix, we show in IV B in a concrete scenario the measurement accuracy of the spin with both a synthetic stellar orbit similar to S2 orbit and one similar to S102/S55.

C. Results on the real data

After testing the validity of our mixed Python/Fortran code using a highly idealized measurement scenario (see Appendix C 3), we use real data to measure the parameters of Galactic Center orbit of S2 and the properties of the black hole as reported elsewhere [12, 13]. Our results agree with their work within systematic and statistical errors. This shows that our code works well with real observations and therefore the validity of using it is assured to calculate several hypotheses in Section IV with real data.

Keck S2 data [12] are used to estimate the parameters assuming the black hole is not free to move relative to us. The best-fit parameters and their 1σ uncertainties are shown in Table I. VLT S2 data in [13] are also used to estimate the parameters, see Table I. The best-fit parameters are consistent with Ghez's and Gillessen's analyses within 2σ and the uncertainties are consistent too. We evaluate how good a model fit is with the chi-square $\chi^2_{\rm dof}$ statistic. The reduced chi-square value $\chi^2_{\rm dof}$ is the chi-square value divided by the number of degree of freedom, which is the degree of freedom of the data subtracted by the number of parameters of the model. Notice that for two measurements that were taken at the same time, the mean of the two measurements of $\{\Delta\alpha_i, \Delta\delta_i\}$ is used as the measurement that happened at that time and the larger error bars are used as the error bars of the observables.

IV. TESTING VARIOUS HYPOTHESES

A. Bayesian hypothesis selection

We assume that the observed orbital data D to have arisen under one of the two hypotheses $\mathcal{H}_0$ and $\mathcal{H}_1$ according to probability density $p(D|\mathcal{H}_0)$ or $p(D|\mathcal{H}_1)$ and for given prior probabilities $p(\mathcal{H}_0)$ and $p(\mathcal{H}_1) = 1 - p(\mathcal{H}_0)$, we obtain from Bayes's theorem

$$p(\mathcal{H}_i|D) = \frac{p(D|\mathcal{H}_i)p(\mathcal{H}_i)}{p(D|\mathcal{H}_0)p(\mathcal{H}_0) + p(D|\mathcal{H}_1)p(\mathcal{H}_1)}, \quad (i = 0, 1) \tag{25}$$

and

$$\frac{p(\mathcal{H}_0|D)}{p(\mathcal{H}_1|D)} = \frac{p(D|\mathcal{H}_0)}{p(D|\mathcal{H}_1)} \frac{p(\mathcal{H}_0)}{p(\mathcal{H}_1)}, \tag{26}$$

TABLE I. Orbital parameters for S2 and the black hole properties with Keck data and VLT data

Parameter (Symbol) [Unit]	Keck best-fit	VLT best-fit	VLT best-fit w/o 2002
Semimajor axis (a) [M_*]	2.45×10^4 ±440	$2.636\times10^4\pm446$	$2.452\times10^4\pm594$
Eccentricity (e)	0.9048 ± 0.0038	0.8953 ± 0.0040	0.9038 ± 0.0060
Initial phase (Φ_0) [radian]	3.178 ± 0.0029	3.031 ± 0.0032	3.038 ± 0.0040
Euler angle 1 (β) [radian]	0.268 ± 0.008	0.186 ± 0.0076	0.227 ± 0.0136
Euler angle 2 (γ) [radian]	1.464 ± 0.013	1.490 ± 0.016	1.444 ± 0.0252
Euler angle 3 (ψ) [radian]	3.936 ± 0.013	4.047 ± 0.012	4.030 ± 0.0120
Distance (d) [kpc]	7.328 ± 0.17	8.422 ± 0.288	7.571 ± 0.382
RA offset of BH ($\Delta\alpha_{bh}$) [radian]	$1.4166\times10^{-8}\pm4.42\times10^{-9}$	$4.99\times10^{-9}\pm3.15\times10^{-9}$	$9.86\times10^{-9}\pm3.34\times10^{-9}$
DEC offset of BH ($\Delta\delta_{bh}$) [radian]	$-4.2962\times10^{-8}\pm6.543\times10^{-9}$	$-1.84\times10^{-8}\pm7.41\times10^{-9}$	$-1.575\times10^{-8}\pm1.026\times10^{-8}$
Mass (M) [$10^6 M_\odot$]	4.468 ± 0.236	4.492 ± 0.244	3.624 ± 0.272
Spin ($\mathbf{J}$)	not measurable	not measurable	not measurable
Reduced chi-square $\chi^2_{\rm dof}$ [1]	1.4	1.0	1.0

The table shows the estimated modes and one-sigma errors of the six parameters of S2 orbits and seven parameters of the Galactic Center black hole from Keck and VLT data using our MCMC code. The best-fit parameters are consistent with Ghez's [12] and Gillessen's [13] analyses within 2σ. The second, third, and fourth rows are the best-fits of the parameters and their uncertainties with Keck data, VLT data, and VLT data subtracted by its data in 2002 to compare with Keck data because Keck does not contain observations in 2002, respectively. We point out the fact that the spin of the black hole is not testable with the two data sets.

where we define the Bayes factor as

$$B_{01}=\frac{p(D|\mathcal{H}_0)}{p(D|\mathcal{H}_1)}. \tag{27}$$

When the two hypotheses are equally probable, the Bayes factor B_{01} is equal to the posterior odds in favor of H_0.

If for $\mathcal{H}_0$ and $\mathcal{H}_1$ we choose models $\mathcal{M}_0$ and $\mathcal{M}_1$ parametrized by model parameter vectors θ_0 and θ_1, we then have to select between the two models using the Bayes factor,

$$B_{01}=\frac{p(D|\mathcal{M}_0)}{p(D|\mathcal{M}_1)}=\frac{\int p(\theta_0|\mathcal{M}_0)p(D|\theta_0,\mathcal{M}_0)d\theta_0}{\int p(\theta_1|\mathcal{M}_1)p(D|\theta_1,\mathcal{M}_1)d\theta_1}, \tag{28}$$

where $p(\theta_i|\mathcal{M}_i)$ is the prior probability distribution function of parameter vector θ_i in $\mathcal{M}_i$ for $i=0,1$.

B. Does the Galactic Center black hole spin?

A measurement of the spin of the Galactic Center black hole is of significant interest. Short of an accurate measurement, one can assess the evidence of the existence of any spin. Working in the framework of General Relativity, we choose the same parameter vector, except the spin, for both the non-spin model ($\mathcal{M}_0$) and the spin model ($\mathcal{M}_1$) that address the S2 orbit around the Galactic Center black hole, i.e., $\theta_0=\{a,e,\Phi_0,\beta,\gamma,\psi,d,\Delta\alpha_{bh},\Delta\delta_{bh},M\}$ and $\theta_1=\{a,e,\Phi_0,\beta,\gamma,\psi,d,\Delta\alpha_{bh},\Delta\delta_{bh},M,\mathbf{J}\}$, and apply Bayesian statistics to answer the question.

Our models $\mathcal{M}_0$ and $\mathcal{M}_1$ are nested, i.e., $\mathcal{M}_1$ reduces to $\mathcal{M}_0$ when the spin J or dimensionless spin $\chi=J/M^2$ acquires 0. For a smooth, marginalized posterior probability distribution $P(J,\mathcal{M}_1|D)$ of spin J for model $\mathcal{M}_1$ that is obtained from an MCMC sampling and has a maximum, we define the 68.3% credible interval to be $\chi\in[\chi_L,\chi_H]$ such that $\int_{\chi_L}^{\chi_H}P(\chi,\mathcal{M}_1|D)d\chi=0.683$ with $P(\chi_L,\mathcal{M}_1|D)=P(\chi_H,\mathcal{M}_1|D)$. For Keck data of S2 orbit up to 2007 in Table 3 in [12] and VLT data up to 2009 in [13], respectively, we use our MCMC code to obtain the posteriors for dimensionless spin χ under the non-zero spin model $\mathcal{M}_1$, and both of the spin posteriors are uniform distributions. It is uninformative about the spin of the Galactic Center black hole with either data set. We also evaluate the Bayes factor B_{01} for the selection of our two models with the Keck data of S2 orbit. So parameter estimation is also done on the non-spin model $\mathcal{M}_0$. The Bayes factor B_{01} in favor of the non-spin model $\mathcal{M}_0$ than the spin model $\mathcal{M}_1$ is 1.2, which is calculated from Eq. (28) with the posteriors from the MCMC samplings with the Keck data for the two models that represent the two hypotheses. As stated at the beginning of this section, the parametrized parameters for the two models are the same except that there is no spin parameter in the non-spin model $\mathcal{M}_0$ and there is the spin parameter $\mathbf{J}$ in the spin model $\mathcal{M}_1$. The value $B_{01}=1.2$ is interpreted as that the non-spin model $\mathcal{M}_0$ is slightly (but barely worth mentioning) more strongly supported by the data than the spin model $\mathcal{M}_1$. We find that this does not contradict with the most recent results on the Galactic Center black hole spin [24] where their estimate is $\chi<0.1$ strictly.

What measurements of star S2 can allow us to constrain the black hole spin? We assume a set of future achievable measurement accuracy $\{\sigma_{\Delta\alpha}=\sigma_{\Delta\delta}=10\ \mu as,\ \sigma_{v_r}=500\ m/s\}$, which are the resolution limits of GRAVITY instrument [47, 48], and use our code to conduct fake/virtual observations of S2 around the Galactic Center black hole and then estimate the model

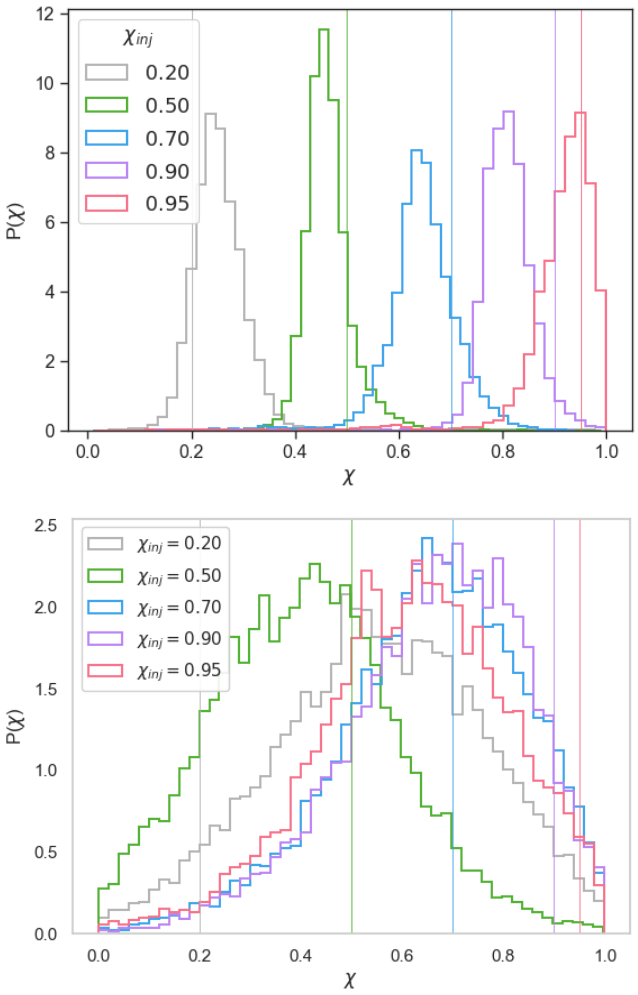

FIG. 2. The marginalized posteriors of dimensionless spin $\chi = J/M^2$ for the fake observations of S2 in Scenario I (top panel) and II (bottom panel) in Table II. The thin vertical lines are injected values. The range of the spin J is $[0, M^2]$, where $M = 1.15M_*$ and $M_* = 4.0 \times 10^6 M_\odot$. The star has an S2-ish orbit. It is observed once per week for 2080 weeks or about 40 years for 2.5 full orbits for the top panel; and twice per week for 1000 weeks or about 20 years for more than one full orbit for the bottom panel. Notice that the inference results of χ for Scenario II is much less informative than that of Scenario I. The measurement uncertainties $\{\sigma_{\Delta\alpha} = \sigma_{\Delta\delta} = 10\ \mu as,\ \sigma_{v_r} = 500\ m/s\}$ are the limits of GRAVITY at a distance of 8 *kpc*.

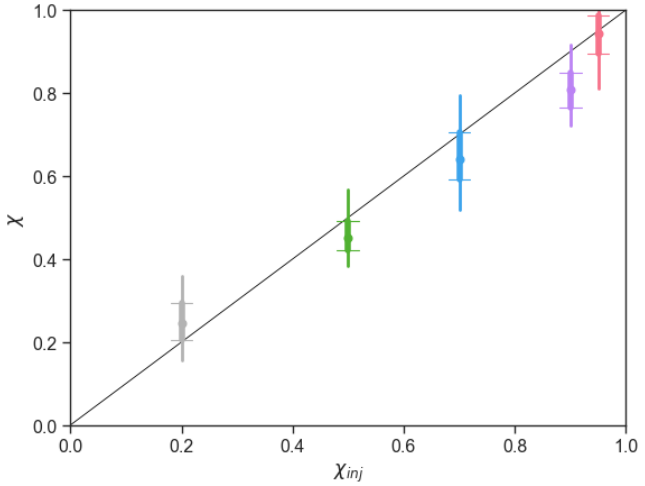

FIG. 3. The mode and two credible intervals of the dimensionless spin χ of the Galactic Center black hole as a function of injected dimensionless spin $\chi_{\rm inj}$ for fake observation Scenario I in Table II and from the top panel of Figure 2. Dots show the maxima of posterior estimates of χ; bars indicate the 68.3% (1σ, thick with caps to the ends) and the 95.4% (2σ, thin) credible intervals. The black thin line is when $\chi = \chi_{\rm inj}$.

parameters including the spin. For each simulation we inject a dimensionless spin value $\chi_{\rm inj} = J_{\rm inj}/M^2$ to the black hole and let the star evolve its orbit around this spinning black hole under the equation of motion model in Eq. (1). To mimic measurements with noise in it, we add a Gaussian noise of the chosen measurement accuracy (Table II) to the evolved stellar orbits for each observable in each measurement/epoch, i.e., the three observables which consist of two angular offsets and one radial velocity. We then use our MCMC code to calculate marginalized posterior distributions of the parameters, including the black hole spin, given the fake observed orbital data D_f. That is $P(\chi|D_f) \propto P(\chi)P(D_f|\chi)$. The prior in χ is flat. The observations are called Scenario I and summarized in Table II. The stellar orbit has $a = 2.65 \times 10^4\ M_*, e = 0.8847, \Phi_0 = -0.1$ (which corresponds to Aug, 2017 for S2, and we assume that is when we start the virtual observations) and three Euler angles that have the values of an S2 orbit. The parameters for the black hole are $M = 4.6 \times 10^6\ M_\odot = 1.15M_*$ and its sky position $d = 8.0\ kpc$, $RA = 265.75°$, and $DEC = -28.79°$ which are determined by the observed S2 orbit. The injected dimensionless spin $\chi_{\rm inj}$ values are $\{0.2, 0.5, 0.7, 0.9, 0.95\}$ and the spin direction is $\{\phi_J = \pi, \cos\theta_J = 0.2\}$ for any of those five injected spin magnitudes. We get from MCMC the marginalized posterior $P(\chi|D_f)$ for the fake observed data with that injected spin value $\chi_{\rm inj}$. We do the same for different injected black hole spin values. The fake observations are conducted once per week for 2080 weeks, or 40 years, about two and a half complete orbits in Scenario I. In Scenario II, we take the same number of measurements but the measurement are arranged twice frequently during half the observing time compared to Scenario I. In Scenario III, we consider a star that orbits around the black hole at half the size of the S2 orbit. We observe it weekly for 800 weeks or about 2.5 full orbits.

The plots in Figure 2 show the marginalized posteriors of χ for different injected values $\chi_{\rm inj}$ for Scenario I (top panel) and Scenario II (bottom panel). Even though they have the same number of data points and the observation are done on the same star S2, the Scenario I has better constraints on the spin than the Scenario II. The

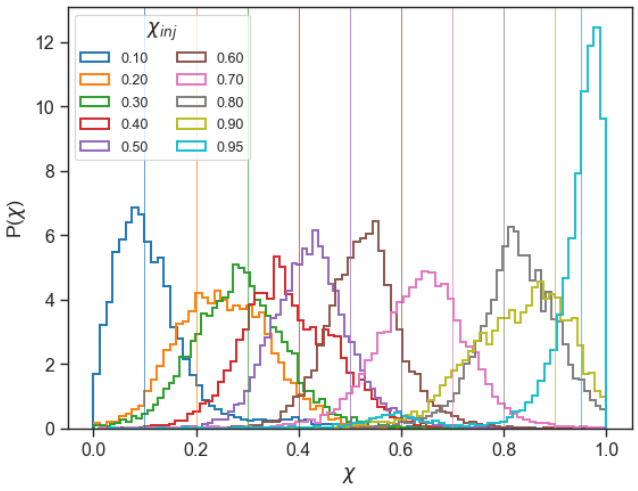

FIG. 4. The marginalized posteriors of dimensionless spin χ for different injected values $\chi_{\rm inj} \in [0, 1]$ in Scenario III in Table II. The vertical thin lines are injected values. The star has an S2-ish orbit except its orbit is half-sized. It is observed once per week for 800 weeks.

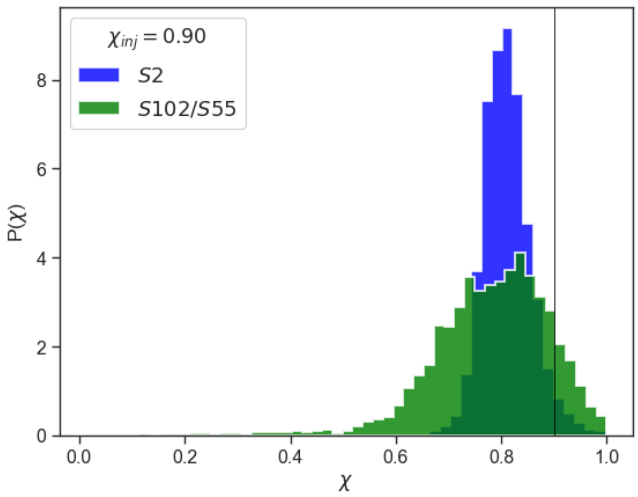

FIG. 5. The marginalized posteriors of dimensionless spin χ for injected value $\chi_{\rm inj} = 0.90$ for S2 (blue) in Scenario I in Table II and S102/S55 (green) in Scenario VI in Table III. The vertical thin lines is injected value. Both stars are observed once per week for 2080 weeks or 40 years. The differences of the two orbits are their eccentricities and the semimajor axises, which are taken the values for S2 and S102/S55.

minimum we should do to be able constrain the black hole with S2 orbit during 40 years, or a person's entire academic career, is to observe it once per week to record the three orbital observables. Observing less frequently or for shorter amount of time will not enable us to constrain the black hole spin decisively. On the other hand, if we can find a star that has an orbit half the size of that of S2, then to achieve a similar measurement accuracy on the spin as in Scenario I, we can take Scenario III where we only need to observe it for less than half of the time (from 40 years to 16 years) at the same measurement frequency. Figure 4 shows the posteriors of χ for Scenario III. Note that for all the cases in the Scenarios I through V, the reduced least-square value $\chi^2_{\rm dof} \approx 1$ which means the sampling is converged.

Now let us look at the parameter estimation posteriors on the black hole spin in a recovered v.s. injected plot. Figure 3 shows the credible intervals of the black hole spin as a function of injected spin value for Scenario I. For each injected value, we plot two error bars. The thick-lined error bar with caps to the two ends is the 68.3% credible interval and the thin-lined error bar without caps is the 95.4% credible interval of the marginalized posterior that corresponds to its injected dimensionless spin $\chi_{\rm inj}$. The big round dot of the same color in that bar is the value of maximum posterior. Recall that the prior on χ is uniform for $\chi \in [0, 1]$. The uncertainty of the measured spin is about 0.1 at the 68.3% credible interval for 40 years of weekly measurement of S2 orbit with GRAVITY's best resolution at Galactic Center. The uncertainty comes from the noise in the orbital data.

We also use Fisher matrix to compare the constraints on the black hole spin with different orbits and different observation strategies in general. From Eq. (B32), we can derive that the uncertainty in spin measurement σ_J (or σ_χ), i.e., the inverse of square root of $\Gamma_{J_a J_b}$, is determined by

$$\sigma_\chi \propto \sigma_J \propto \frac{a^2 \sigma_r}{\sqrt{NT}} \frac{(1-e^2)^{\frac{3}{2}}}{(13e^4+9e^2+3)^{\frac{1}{4}}}, \qquad (29)$$

where a is the semimajor axis, e is the eccentricity, σ_r is the stellar orbit measurement accuracy, T is the duration of observation time, and N is the number of measurements. We now use Fisher matrix to check against the MCMC method, with stellar orbits similar to those of S2 and S102/S55 in fake observation Scenarios I and VI, see Figure 5. In this scenario, both stars are observed with the same number of measurements N, the same stellar orbit measurement accuracy σ_r, and the same duration of observation T. The dimensionless spin uncertainty σ_χ, is then scaling only to the semimajor axis a and the eccentricity e. The closer the orbit and the larger the eccentricity, the more accurate we can constrain the black hole spin. Plugging into the values of those two quantities for the two stars respectively from Tables II and III, we can obtain the dimensionless spin uncertainty ratio constrained from the orbits of S2 to S102/S55 using the analytic Fisher matrix for any black hole spin value. It is 0.34. This is consistent with Figure 5, where the uncertainty ratio is $0.129/0.267 \approx 0.48$ based on 95.4% confidence intervals (2-σ errors) for a specific case $\chi_{\rm inj} = 0.9$.

This example uses both the Fisher matrix and the MCMC methods. In general, with Fisher matrix, we know from Eq. (29) that orbits with smaller semimajor axis and larger eccentricity provide better constraints on the black hole spin. From Eq. (29), we know that with

TABLE II. Scenario I: Fake Observation of S2

Parameter (Symbol) [Unit]	Injected parameter value
Star	S2
Semimajor axis (a) [M_*]	2.65×10^4
Eccentricity (e)	0.8847
Initial phase (Φ_0) [radian]	-0.100 (Aug 2017)
Euler angle 1 (β) [radian]	0.169
Euler angle 2 (γ) [radian]	1.515
Euler angle 3 (ψ) [radian]	4.046
Dimensionless spin ($\chi_{\rm inj}$)	$\{0.2, 0.5, 0.7, 0.9, 0.95\}$
Spin angle 1 (ϕ_J)	π
Spin angle 2 ($\cos\theta_J$)	0.200
Quadrupole moment Q_2	$-J_{\rm inj}^2/M$ with $J_{\rm inj} = \chi_{\rm inj} M^2$
Mass (M) [$M_\odot$]	4.60×10^6
Distance (d) [kpc]	8.00
RA of BH (α_{bh}) [degree]	265.754795
DEC of BH (δ_{bh}) [degree]	-28.794375
Measurement uncertainty in RA offset ($\sigma_{\Delta\alpha}$) [μas]	10
Measurement uncertainty in DEC offset ($\sigma_{\Delta\delta}$) [μas]	10
Measurement uncertainty in radial velocity (σ_{v_r}) [m/s]	500
Orbital period (T) [week]	823
Measurements	2080 weekly

The table lists the injected parameters and observation strategy for the fake observation of star S2 in Scenario I. The posteriors from parameter estimation are shown in the top panel of Figure 2. Here $M_* = 4 \times 10^6 M_\odot$ is used as a scale of black hole mass.

TABLE III. Summary of Fake Observation Scenarios on S2 and future stars

Scenario	Star	Semimajor axis [M_*]	Injected spin $\chi_{\rm inj}$	Period [week]	Measurements
Scenario I	S2	2.65×10^4	$\{0.2, 0.5, 0.7, 0.9, 0.95\}$	823	2080, weekly
Scenario II	S2	2.65×10^4	$\{0.2, 0.5, 0.7, 0.9, 0.95\}$	823	1040×2, semiweekly
Scenario III	Star of half S2 orbit	1.325×10^4	$\{0.1, 0.2, ..., 0.8, 0.9, 0.95\}$	291	800, weekly
Scenario IV	S2	2.65×10^4	$\{0.7\}$	823	2080×7, daily
Scenario V	Star of one fifth S2 orbit	5.3×10^3	$\{0.2, 0.5, 0.7, 0.9, 0.95\}$	73.6	1040, weekly
Scenario VI	S102/S55-ish	2.3×10^4	$\{0.9\}$	665	2080, weekly

Summary of the differences among the four fake observation scenarios. For the parameters that are not specified for Scenarios II, III, IV, V, and VI here, they take the same values as in Scenario I in Table II except that for Scenario VI the eccentricity is $e = 0.721$. The estimated posteriors are shown in the top and the bottom panels of Figure 2 for Scenarios I and II, Figure 4 for Scenario III, Figure 6 for Scenario V, and Figure 5 for Scenario VI.

the same semimajor axis a, which translates to the same orbital period P with Kepler's third law, larger eccentricity (highly eccentric orbits) can constrain the black hole spin more precisely given the same observation strategy. This is because with the same semimajor axis, the pericenter of the more eccentric orbit is closer to the black hole and thus more impacted by the black hole's gravitational wave potential. This is why S2 can provide better constraints (as is the case in our simulation shown in Figure 5) on the black hole spin than what S102/S55 can do, even though S102/S55 has a shorter period.

Similarly, from Eq. (29), we can see that if we cannot observe S2 for 40 years weekly in order to determine the black hole spin, which is most likely, the solution is to find a closer or improve the instrument measurement precision. It is worth pointing out that if we have N stars whose orbits are similar to S2 and we observe each of them equally frequently and for the same amount of time duration, we are expected to see an improvement of a factor of $\sqrt{N}$ in the measurement uncertainty of black hole spin.

C. Testing no-hair theorem

According to the black hole no-hair theorem, a black hole is completely characterized by its mass M, angular momentum (or spin) J, and charge q. For an astrophysical black hole which is electrically neutral, it is fully described by two quantities, M and J. As a consequence, the quadrupole moment Q_2 of its external spacetime is given by $Q_2 = -J^2/M$. The quadrupole moment can cause the stellar orbits around the black hole to precess, and the precession rate is on the order of 1 μas. for

a highly eccentric orbit around the Galactic Center supermassive black hole with orbital period of years. This makes it possible to use the stellar orbit data from the modern infrared telescopes to test the no-hair theorem. In reality, there is perturbing external quadrupole moment Q_X (see Section II, V) due to the S star cluster, dark matter, and intermediate-mass black holes that are close to the Galactic Center. This should also be taken into consideration. In this study, we employ the most optimistic possible scenario, equivalent to perfect knowledge of any external tidal potential.

In order to test the no-hair theorem, we apply our MCMC code to the VLT orbital data of S2 we can obtain the marginalized posterior probabilities of spin J and quadrupole moment Q_2, which are both flat. The existing data are not sufficient for us to draw a conclusion on the no-hair theorem. This is not surprising because we cannot even constrain spin yet.

What observation strategy on S2 will enable us to test the no-hair theorem in the future? Applying the same method that is used in Section IV B, we conduct fake observations of S2 again. Specifically, we first do Scenario IV. The injected parameters and the observing strategy can be found in Table III and its reference Table II. We use our code to generate fake observed orbital data points with noise in them for S2 star around our Galactic Center for an injected black hole spin $\chi_{\rm inj} = 0.7$ and quadruple moment $Q_{2,\rm inj} = 0.648$. This simulates the real observation scenario. We virtually observe the star once per day for 2080 weeks, which is nearly 40 years and about 2.5 full orbits. We then use MCMC to obtain the marginalized posterior probability distribution of Q_2 for the choice of the $\chi_{\rm inj}$ and the $Q_{2,\rm inj}$ values. In the parameter estimation, Q_2 is treated as an independent parameter on J and M, so it does not follow $Q_2 = J^2/M$. For this set up, it is equivalent to see how well the quadrupole term Q, including external quadrupole moment Q_X, can be constrained. The posteriors $p(Q_2)$ for different injected values are all flat. This means, we cannot constrain the quadrupole term or the no-hair theorem even if we observe S2 daily for 40 years with the measurement accuracy limits of GRAVITY telescope. This is mainly because at a periapsis of about 120 AU or 2800 times the mass of the black hole, the star is not close enough to the supermassive black hole so as to be significantly affected by the black hole's quadrupole moment. In order to use S2 to constrain Q_2, we will have to improve our angular measurement accuracy, compared to GRAVITY's limits, by at least two orders of magnitude and the radial velocity accuracy by one order of magnitude from our virtual experiments. We point out that Fisher matrix is not used in this case. With Fisher matrix we only worked in the coordinates whose origin is at the center of black hole. See the toy model in Appendix C 3. However, we used the conclusion from Fisher matrix study that by observing N times as often, we can improve the measurement error bars of spin by a factor of $\sqrt{N}$ to guide our numerical simulation in terms of observation strategy choices.

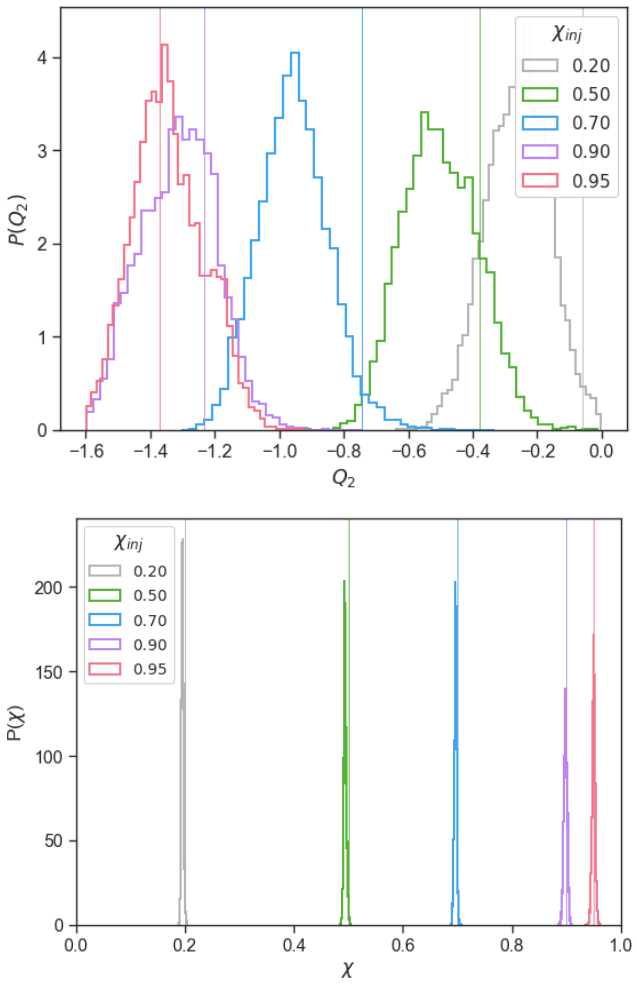

FIG. 6. Posteriors of Q_2 and χ for Scenario V in Table III. The thin vertical lines are injected values. The top panel shows the marginalized posteriors of quadrupole Q_2 for different injected values $\chi_{\rm inj}$ and their corresponding injected quadruple values $Q_{2,\rm inj} = -\chi^2_{\rm inj} M^3$. The bottom panel for the posteriors of the dimensionless spin χ. The star has an orbit that is one fifth the semimajor axis of S2. It is observed twice per week for about seven full orbits.

Because S2 with even GRAVITY will not work, what kind of stellar orbits and observation strategy do we need to test the no-hair theorem then? The next generation of extremely large telescopes will discover stars with orbital periods as small as 1-2 years given their increased sensitivity and angular resolution [34]. We assume that we are lucky enough to find a star orbiting around the Galactic Center with an orbit that has a quarter of the semimajor axis of S2 ($\sim$ 200 AU) and all the other orbital parameters the same as S2. This star has an orbital period of 73.6 weeks and we observe it once per week for 1040 weeks (20 years and 14 full orbits) in our simulation Scenario V, see Tables III and II. With this fake observation scenario, we can start to measure the quadrupole moment Q_2 for different injected Q_2inj. See the top panel of Figure 6 for

the posteriors $P(Q_2)$. In this figure, also plotted is the measurement of dimensionless spin χ for various injected values in the bottom panel. We can see that while the Q_2 can be measured to a visually distinguishable extent, the black hole spin can be measured at a very high accuracy, ~ 0.01. As an example, we show in Figure 7 the corner plot of posteriors of all modeled parameters for a specific case, $\chi_{\rm inj} = 0.900$ and $Q_{2,\rm inj} = 1.232$ in Scenario V.

V. CONCLUSIONS

We have introduced a Markov chain Monte Carlo method to constrain the Galactic Center black hole properties with a model of the Galactic Center stellar orbits. We also use Fisher matrix method to check against MCMC when the scenarios allow. Three main conclusions come out of this work.

First, we conclude that we are not able to constrain the black hole spin or test the no-hair theorem with the existing data of S2 stellar orbit from Keck and/or VLT measurements taken from 1995 to 2007 (2009 for VLT).

We also give strategies for future observations on how to constrain the black hole spin with S2 orbit based on simulated fake observation scenarios, assuming future achievable measurement accuracy. With the best measurement uncertainty by the GRAVITY telescope when it observes at an angular accuracy of 10 μas (mircroarcsecond) and a radial velocity accuracy of 500 m/s, we can constrain the black hole spin at 0.1 accuracy and precision if S2 is observed once per week for 40 years as shown in Figure 2 for Scenario I in Table II. If we can find a closer star that is half the size of S2 orbit, then the total observing time and frequency required to reach the 0.1 precision in the dimensionless spin will be reduced as shown in Figure 4 for Scenario III in Table III. We also derive an analytic expression to scale the uncertainty of the spin measurement using Fisher matrix in terms of the observation strategy, the star's orbital parameters, and the instrument precision, see Eq. (29).

On the black hole no-hair theorem, it is concluded that with S2 orbit we are not able to test the theorem even with 40 years daily measurements using GRAVITY's measurement limit of S2 orbit in Scenario IV in Table III. In order to test the no-hair theorem with GRAVITY's best resolution, we need a closer star. It is expected to find stars with orbital periods of 1-2 years by the next generation large telescopes [34]. In our simulations we use a star that is one fifth the distance to the Galactic Center than S2 and has other orbital parameters similar to that of S2 such that the orbit can be influenced more by the spin and the quadrupole moment that characterize the black hole's gravitational potential. With such a star, we can start to measure the quadrupole moment and test the black hole no-hair theorem with 20 years of weekly observations as shown in Figure 6 for Scenario V in Table III. It is necessary to understand the distribution of visible and dark matter outside the black hole to better constrain the no-hair theorem; however, without such knowledge, we can treat the quadrupole moment as an independent parameter on the black hole spin and a term that combines the quadrupole moment of both the black hole and the external sources in the vicinity of Sgr A*, and see how well we can measure it as shown in Figure 6.

Several other scenarios can be further studied based on our investigation. The epochs of the observations are equally spaced in our simulations. If these measurements are rearranged such that they are more frequently made when the star is close to the periapsis of its orbit around the black hole than the apoapsis, the parameter measurement uncertainties in the model are expected to reduce. One factor that can be changed in future scenarios is the instrumental measurement accuracy. In this work it is chosen to be the limits of GRAVITY telescope for all our fake observations we present, but if the measurement accuracy can be further improved, we can have improved observation strategies with less observation time to test the black hole no-hair theorem. Besides, if several more closer stellar orbits are found then we can use them to jointly constrain the black hole properties.

Another direction to explore is to use the radio images of supermassive black holes. The Event Horizon Telescope measurements are complementary to stellar proper motions and therefore could break some degeneracies and make constraints on the black hole nature of the central remnant easier [4–9].

Existing observations do not provide enough information to constrain the ambient density of perturbers, which can impact our interpretation of these orbits. Dynamical processes have long been expected to produce a high density of nearby massive objects, as yet inaccessible to direct electromagnetic observation [21, 49–54]. This dark density is most likely to be constrained indirectly, via its gravitational effects (e.g., [54], though [55]). Anisotropies in the ambient density can partially mimic the effects of modified theories of gravity; for example, a quadrupolar gravitational perturbation could be sourced by the black hole or an external cluster density.

ACKNOWLEDGMENTS

We thank Phil Chang for extensive help with the Fortran orbit evolution solver which crucially speeds up the code, and Clifford Will for useful discussions on the project. The project was supported by the STFC grant ST/T000147/1. We are grateful for the computational resources that were supported by NSF-0923409 and provided by the Leonard E Parker Center for Gravitation, Cosmology and Astrophysics at University of Wisconsin-Milwaukee, where Hong conducted most of the calculations for this work as a graduate student.

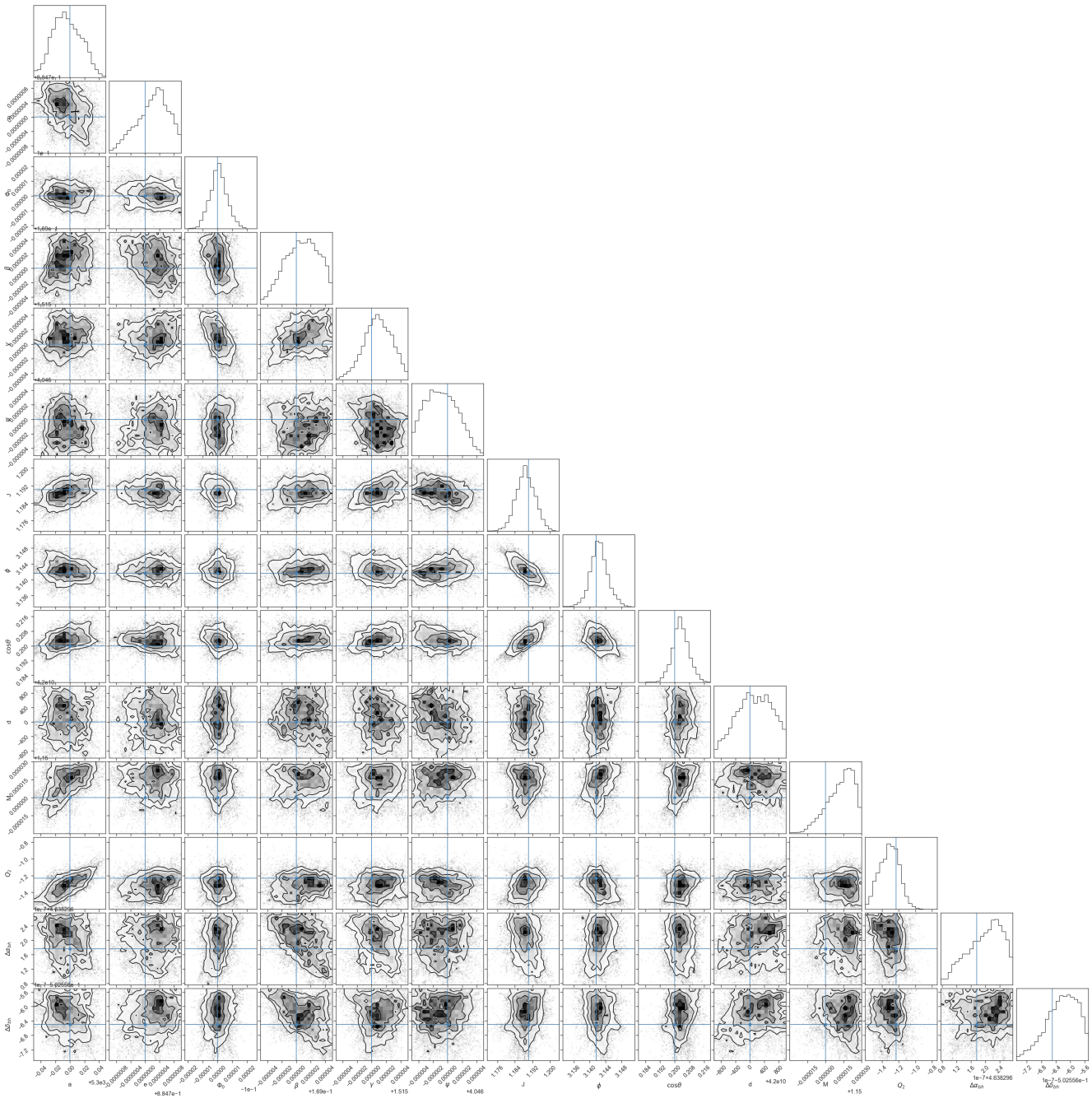

FIG. 7. Corner plot for the posterior distributions of the parameters for the case of injected $\chi_{\rm inj} = 0.900$ and $Q_{2,\rm inj} = 1.232$ in Scenario V in Table III.

Appendix A: Equations of motion

In this appendix, we point out that different properties of an ensemble of stellar orbits probe different physics. For example, the orbit location probes different parts of the potential: distant orbits preferentially probe an external potential while nearby orbits probe the black hole. Similarly, different symmetry-breaking effects only occur from certain physical processes; for example, spherically symmetric potentials cannot cause the orbital plane to precess, while quadrupolar Newtonian potentials and frame dragging cause an ensemble of orbits to evolve in distinctly different ways. By isolating these symmetries and their impact on observations, we can easily model how a collection of measurements of several stellar orbits can best constrain properties of the Galactic Center environment.

In the text, we adopted simple approximations to general relativity at low post-Newtonian order, neglecting many common factors like the mass ratio. Because orbital perturbations we hope to identify are small, influences from small factors like mass ratio ($\simeq 10^{-6}$) can be of similar order to the minute effects we seek to identify at targeted separations. For this reason, in this section we carefully review relevant post-Newtonian expressions, targeting typical separations (i.e., 10 year orbits) and post-Newtonian accuracy ideally comparable to the targeted astrometric resolution of $\mu as/yr$ at 8 kpc (i.e., $\simeq 0.26 Myr$, or $\Delta v/c \simeq 10^{-7}$).

Post-newtonian theory for binary and N-body motion is well-developed; see [38] for a review in the context of stellar orbits around supermassive black holes; [56] for a discussion of orbit-averaged spin-precession; and [57], [39] for technically sophisticated and highly detailed discussions in general and for binary motion, specifically.

1. Post-Newtonian Two-body equations of motion

Working to v^2 (1PN) beyond Newtonian order in velocity and leading-order in spin-orbit coupling, the post-Newtonian Lagrangian for two-body motion has the form [38]

$$\mathcal{L} = \eta M \left[\frac{1}{2}v^2 + \frac{GM}{r} + \frac{1}{8}(1-3\eta)v^4 + \frac{GM}{2r}(3+\eta)v^2 + \eta\dot{r}^2 - \frac{GM}{r}\right] + \mathcal{L}_{spin} + \mathcal{L}_{quad}, \tag{A1}$$

using units with $c = 1$ for simplicity. Here $\mathcal{L}_{spin}$ and $\mathcal{L}_{quad}$ terms are due to the black hole spin and the quadrupole moment. The Lagrangian corresponds to the Hamiltonian [58]

$$H = \mu[H_N + H_{1PN} + H_{SO}] \tag{A2}$$

$$H_N = \frac{p^2}{2} - \frac{M}{r} \tag{A3}$$

$$H_{1PN} = \frac{1}{8}(3\eta - 1)p^4 - \frac{1}{2}[(3+\eta)p^2 + \eta p_r^2]\frac{M}{r} + \frac{M^2}{2r^2} \tag{A4}$$

$$H_{SO} = 2\frac{\mathbf{L}_N/\mu \cdot \mathbf{J}}{r^3}. \tag{A5}$$

These approximations, plus the limit $\eta \to 0$, reproduce the equations of motion adopted in the text. These Hamiltonian expressions also enable straightforward derivation of the orbit-averaged precession equations. As a concrete example, the contribution of black hole spin to the orbit-averaged precession equations for L_N, A_N follow from the Lie algebra

$$(\partial_t L_a)_{SO} = \{L_a, H_{SO}\} = \frac{2\epsilon_{abc}J_b L_c}{r^3} \tag{A6}$$

$$\begin{aligned}(\partial_t A_a)_{SO} &= \{(p\times L - M\hat{r})_a, H_{SO}\} \\ &= \left\{(p\times L - M\hat{r})_a, \frac{1}{r^3}\right\}(2\vec{J}\cdot\vec{L}) + \{(p\times L - M\hat{r})_a, L_d\}2J_d/r^3 \\ &= -3\frac{\epsilon_{abc}r_b L_c}{r^5}(2\vec{J}\cdot\vec{L}) + \epsilon_{abc}\frac{2J_b}{r^3}A_c,\end{aligned} \tag{A7}$$

using $\{L_a, V_b\} = \epsilon_{abc}V_c$ for any vector V rotating with L (here, $\vec{L}, \vec{p}, \vec{r}$). Both orbit averages can be performed trivially, substituting $\vec{r} = p(\hat{x}\cos\theta + \hat{y}\sin\theta)/(1 + e\cos\theta)$ and $dt = d\theta L/r^2$ for the special case $\vec{A} = e\hat{x}$; we find

$$\left\langle r^{-3}\right\rangle = \frac{2\pi}{P}\frac{M}{p^3} \tag{A8}$$

$$\left\langle r\cos\theta r^{-5}\right\rangle = \frac{2\pi}{P}\frac{eM}{p^3}. \tag{A9}$$

Critically, the second term does *not* orbit-average to zero. We therefore find

$$\langle(\partial_t A)_{\rm SO}\rangle = \frac{2M}{p^3}\left[\vec{J} - 3(\vec{J}\cdot\hat{L})\hat{L}\right]\times A. \tag{A10}$$

Are these approximations adequate? First and foremost, as emphasized in the text, most post-Newtonian and mass ratio effects do not break symmetry in a way that can be confused with the influence of precession: even if they *did* matter quantitatively, they wouldn't matter qualitatively. Second, for a *single* star, the back-reaction of the star on the

BH's orbit is small at typical high mass ratio ($\eta \simeq 10^{-6}$); the leading-order effect is purely Newtonian, corresponding to orbits around the center of mass; and higher-order PN effects are suppressed by $O(v^2) \simeq M/r \simeq 10^2 - 10^3$. For a single star, the finite mass ratio is a minute perturbation at separations where precession can be measured astrometrically; see 1.

As emphasized in the text, however, this modification does not break symmetry and therefore does not significantly influence the quantitative accuracy to which precession-induced modulations can be measured.

2. Post-Newtonian N-body equations of motion

When many bodies are included, we must carefully account for the often significant perturbations from neighboring stars, as well as the collectively weakly significant reaction of the black hole to the ambient stellar potential.

Finally, the BH spin will precess to conserve total angular momentum as the stars precess [38] due to Lens-Thirring effects, as well due to the ambient gravitational potential [59]. As the spin precesses, the leading-order spin-orbit precession will be modulated, an effect that can be comparable to quadrupolar precession effects from the central supermassive black hole.

Appendix B: Fisher matrix for Newtonian orbits

To constrain properties of the Galactic Center, we must first identify the Newtonian orbit. In this section we review how to calculate the Fisher matrix for Newtonian orbital parameters using our toy-model likelihood equation for special cases and in relative generality.

1. Fisher matrix for Keplerian orbits

In the discussion above, we adopted as coordinates the initial velocity and position. This choice of coordinates is particularly compatible with our equations of motion and subsequent analytic calculations (e.g., including non-Newtonian perturbations). While straightforward for brute-force calculations, the above approach is rarely analytically tractable. Alternatively, the perturbed orbit Δr can be reduced to (a) changes of a, e and the Newtonian orbital phase Φ_0 and (b) changes in the orientation of the orbit. Using the chain rule, we can build up the total perturbation as an additive contributions from both factors, each individually simple and particularly tractable in suitable coordinates.

Specifically, using as coordinates the orientation of the orbital frame (3 parameters) as well as a, e, Φ_0 (3 parameters), we can express

$$\Delta\vec{r}(t) = \vec{C}_a(t)\Delta a + \vec{C}_e\Delta e + \vec{C}_\Phi\Delta\Phi_0 + (-i\mathcal{L}_\beta\vec{r})\Delta\Theta^\beta, \tag{B1}$$

where $C_{\alpha,X}$ for $\alpha = x, y, z$ are the Cartesian components of the vectors $\vec{C}_X$ and where $\Delta\Theta^\beta$ is a small (constant) rotation vector and $\mathcal{L}_\alpha$ are the generators of rotations. As a concrete example, for circular orbits $\vec{r} = a[\cos(\Omega_N T)\hat{x} + \sin(\Omega_N T)\hat{y}]$, with T as the observation time and Ω_N the rotation rate of the star

$$\vec{C}_a = \hat{r} + \frac{\partial\Omega_N}{\partial a}Ta\hat{v} \tag{B2}$$

$$\vec{C}_\Phi = a\hat{v} \tag{B3}$$

$$\vec{C}_e = 0.5a\{[-3 + \cos(2\Omega_N T)]\hat{x} + \sin(2\Omega_N T)\hat{y}\} \tag{B4}$$

$$-i\mathcal{L}_x\vec{r} = [\hat{y}\hat{z} - \hat{z}\hat{y}]_{ab}\vec{r}_b = -a\hat{z}(\hat{r}\cdot\hat{y}) \tag{B5}$$

$$-i\mathcal{L}_y\vec{r} = [-\hat{x}\hat{z} + \hat{z}\hat{x}]_{ab}\vec{r}_b = a\hat{z}(\hat{r}\cdot\hat{x}) \tag{B6}$$

$$-i\mathcal{L}_z\vec{r} = [\hat{x}\hat{y} - \hat{y}\hat{x}]_{ab}\vec{r}_b = a\hat{x}(\hat{r}\cdot\hat{y}) - a\hat{y}(\hat{r}\cdot\hat{x}) = -a\hat{v}, \tag{B7}$$

and rotations around z are degenerate with the change in orbital reference phase Φ_0.

In terms of these coordinates, the Fisher matrix for the idealized measurements in Eq. (C1) can be expressed in the particularly analytically tractable form

$$\Gamma_{\alpha\beta} = \frac{N}{\sigma_r^2}\begin{bmatrix} \int\frac{dt}{T}\sum_b C_{b,a}C_{b,a} & \int\frac{dt}{T}\sum_b C_{b,a}C_{b,e} & \int\frac{dt}{T}\sum_b C_{b,a}C_{b,\Phi} & \int\frac{dt}{T}\sum_b C_{b,a}[-i\mathcal{L}_\beta\vec{r}]_b \\ \int\frac{dt}{T}\sum_b C_{b,e}C_{b,a} & \int\frac{dt}{T}\sum_b C_{b,e}C_{b,e} & \int\frac{dt}{T}\sum_b C_{b,e}C_{b,\Phi} & \int\frac{dt}{T}\sum_b C_{b,e}[-i\mathcal{L}_\beta\vec{r}]_b \\ \int\frac{dt}{T}\sum_b C_{b,\Phi}C_{b,a} & \int\frac{dt}{T}\sum_b C_{b,e}C_{b,\Phi} & \int\frac{dt}{T}\sum_b C_{b,\Phi}C_{b,\Phi} & \int\frac{dt}{T}\sum_b C_{b,e}[-i\mathcal{L}_\beta\vec{r}]_b \\ \int\frac{dt}{T}\sum_b C_{b,a}[-i\mathcal{L}_\beta\vec{r}]_b & \int\frac{dt}{T}\sum_b C_{b,e}[-i\mathcal{L}_\beta\vec{r}]_b & \int\frac{dt}{T}\sum_b C_{b,\Phi}[-i\mathcal{L}_\beta\vec{r}]_b & \int\frac{dt}{T}[\mathcal{L}_\alpha\vec{r}]\cdot[\mathcal{L}_\beta\vec{r}] \end{bmatrix}. \tag{B8}$$

We confirm this representation reproduces the results provided above. Being analytically tractable even for eccentric orbits, this general form is particularly well-suited to marginalization via Eq. (24).

For circular orbits, the expressions involved can be approximately evaluated, using the following rules

$$\langle \hat{r}_a \hat{r}_b \rangle = \frac{1}{2}[\delta_{ab} - \hat{L}_a \hat{L}_b] \tag{B9}$$

$$\langle \hat{v}_a \hat{v}_b \rangle = \frac{1}{2}[\delta_{ab} - \hat{L}_a \hat{L}_b] \tag{B10}$$

$$\langle \hat{r}_a \hat{v}_b \rangle = 0, \tag{B11}$$

and by applying these rules, we find the expressions for the Fisher matrix components:

$$\Gamma_{aa} = \frac{N}{\sigma_r^2} \int \frac{dt}{T} \sum_b C_{b,a} C_{b,a} = \frac{N}{\sigma_r^2} \int \frac{dt}{T} (1 + t^2 a^2 (\partial \Omega_N / \partial a)^2) \tag{B12}$$

$$\Gamma_{\Phi\Phi} = \frac{N a^2}{\sigma_r^2} \tag{B13}$$

$$\Gamma_{ee} = \frac{5 N a^2}{2 \sigma_r^2} \tag{B14}$$

$$\Gamma_{ae} = 0 \tag{B15}$$

$$\Gamma_{a\Phi} = \Gamma_{a\Theta_z} = \frac{N}{\sigma_r^2} \int \frac{dt}{T} t a^2 (\partial \Omega_N / \partial a) \tag{B16}$$

$$\Gamma_{e\Phi} = 0 \tag{B17}$$

$$\Gamma_{\Theta_x a} = \Gamma_{\Theta_y a} = \Gamma_{\Theta_x e} = \Gamma_{\Theta_y e} = \Gamma_{\Theta_x \Phi} = \Gamma_{\Theta_y \Phi} = 0 \tag{B18}$$

$$\Gamma_{\Theta_x \Theta_x} = \Gamma_{\Theta_y \Theta_y} = \frac{N a^2}{2 \sigma_r^2} \tag{B19}$$

$$\Gamma_{\Theta_y \Theta_y} = \frac{N a^2}{\sigma_r^2} \tag{B20}$$

$$\Gamma_{\Phi \Theta_z} = -\frac{N a^2}{\sigma_r^2}. \tag{B21}$$

The terms in this circular-orbit Fisher matrix have qualitatively different behavior. On the one hand, changes in the orbital period (a) lead to significant, increasing dephasing across multiple orbits; as a result, the orbital radius can be measured with high accuracy, increasing rapidly as the measurement interval increases [$\Gamma_{aa} \propto (\omega T)^2 N (a/\sigma_r)^2$]. By contrast, all other changes in a circular orbit are *geometrical*, producing *small or variable* separations. While our ability to measure these parameters also increases with the number of measurements ($\propto N \propto T$), the accuracy to which these parameters can be measured is significantly smaller. Finally, the circular-orbit Fisher matrix decomposes trivially into diagonal terms (almost all) plus one 2×2 block ($\ln a, \Phi$); this nearly-degenerate 2×2 block can be trivially diagonalized

$$\Gamma_{ab} = \frac{N a^2}{\sigma_r^2} \begin{bmatrix} 1 + \frac{T^2}{3} a(\partial_a \Omega)^2 & \frac{T}{2} a(\partial_a \Omega) \\ \frac{T}{2} a(\partial_a \Omega) & a^2 \end{bmatrix} = \frac{N a^2}{\sigma_r^2} \begin{bmatrix} 1 + \frac{3}{4}\Phi_{orb}^2 & -\frac{9}{8}\Phi_{orb} \\ -\frac{9}{8}\Phi_{orb} & \frac{9}{4}\Phi_{\rm orb}^2 \end{bmatrix} \tag{B22}$$

using $T a \partial_a \Omega_N = -3\Phi_{orb}/2$ for $\Phi_{orb} = \Omega_N t$ the orbital phase. The relative significance of the two terms depends on how many orbital cycles have occurred.

2. Unknown black hole mass

Adding additional parameters, like the black hole mass, is straightforward:

$$\Delta \vec{r}(t) = \textstyle\sum_A \vec{C}_\lambda \Delta\lambda. \tag{B23}$$

For circular orbits, the effect of a perturbed black hole mass is *very similar* to a perturbed orbital separation, producing a significant dephasing with time without any (small) change in position:

$$\vec{C}_M = \tfrac{\partial \Omega_N}{\partial M} t a \hat{v}. \tag{B24}$$

Because the Newtonian orbital period only depends on $\sqrt{M/a^3}$, these two parameters are nearly degenerate in the Fisher matrix: we can only measure one combination (the orbital period!) reliably. Marginalizing out the unknown orbital radius a, we find the Fisher matrix for black hole parameters does *not* depend as sensitively on the stellar mass. For circular orbits specifically, all parameters except M, a, Φ separate, allowing us to marginalize only a 3-dimensional matrix

$$\Gamma_{MM} = \frac{Na^2t^2}{3\sigma_r^2}\left(\frac{\partial\Omega_N}{\partial M}\right)^2. \tag{B25}$$

3. Unknown black hole spin

The black hole spin enters via $\vec{\Omega}$ in a particularly simple way at leading order: $\partial\Omega^\alpha/\partial J_\beta = \delta^\alpha_\beta Z_J$. For example, the Fisher matrix over J components has the form

$$\begin{aligned}
\Gamma_{\alpha\beta} &= \frac{N}{\sigma_r^2}\int\frac{dt}{T}\frac{\partial\Omega^a}{\partial J^\alpha}\frac{\partial\Omega^b}{\partial J^\beta}\left\langle t^2[\mathcal{L}_a r_o]\cdot[\mathcal{L}_b r_o]\right\rangle \\
&\simeq \frac{N}{\sigma_r^2}\frac{\partial\Omega^a}{\partial J^\alpha}\frac{\partial\Omega^b}{\partial J^\beta}\frac{T^2}{3}\mathrm{Tr}[\mathcal{L}_a I\mathcal{L}_b^T] \\
&\simeq \frac{NZ_J^2T^2}{3\sigma_r^2}\int_0^P\frac{dt}{P}\mathrm{Tr}[\mathcal{L}_a I\mathcal{L}_b^T] \\
&= \frac{NZ_J^2T^2[a(1-e^2)]^4}{3\sigma_r^2PL}\mathrm{Tr}[\mathcal{L}_a(A_1\hat{x}\hat{x}+(A_2-A1)\hat{y}\hat{y})\mathcal{L}_b^T],
\end{aligned} \tag{B26}$$

where

$$A_1 \equiv \int_0^{2\pi} d\theta\ \frac{\cos^2\theta}{(1+e\cos\theta)^4} = \frac{(1+4e^2)\pi}{(1-e^2)^{7/2}} \tag{B27}$$

and

$$A_2 \equiv \int_0^{2\pi} d\theta\ \frac{1}{(1+e\cos\theta)^4} = \frac{(2+3e^2)\pi}{(1-e^2)^{7/2}}. \tag{B28}$$

Both integrals can be performed analytically when T/P is an integer; in this special case we find

$$A_2 \simeq \frac{T}{P}\int_0^{2\pi} d\theta\frac{1}{(1+e\cos\theta)^4} = 2\pi T/P\frac{(1+\frac{3}{2}e^2)}{(1-e^2)^{7/2}} \tag{B29}$$

$$A_1 = \pi T/P\frac{1+4e^2}{(1-e^2)^{7/2}}. \tag{B30}$$

Using the explicit form of the generators $\mathcal{L}$ in this frame, we find the trace

$$\mathrm{Tr}[\mathcal{L}_a(A_1\hat{x}\hat{x}+(A_2-A1)\hat{y}\hat{y})\mathcal{L}_b^T] = \begin{bmatrix} A_2-A_1 & 0 & 0 \\ 0 & A_1 & 0 \\ 0 & 0 & A_2 \end{bmatrix}. \tag{B31}$$

The $\Gamma_{J_a J_b}$ components are then a coefficient times a matrix, and the other matrix components are expressed as following

$$\Gamma_{J_a J_b} = \frac{2NT^2(1-e^2)^{1/2}}{3\pi\sigma_r^2 a^4}\begin{bmatrix} A_2 - A_1 & 0 & 0 \\ 0 & A_1 & 0 \\ 0 & 0 & A_2 \end{bmatrix} \tag{B32}$$

$$\Gamma_{aJ_x} = \frac{4\pi NT^2}{\sigma_r^2 a^5} Tr[(J_x\mathcal{L}_x + J_y\mathcal{L}_\dagger + J_z\mathcal{L}_z)[\hat{x}\hat{x} + \hat{y}\hat{y}]\mathcal{L}_x^T] \tag{B33}$$

$$\Gamma_{aJ_y} = \frac{4\pi NT^2}{\sigma_r^2 a^5} Tr[(J_x\mathcal{L}_x + J_y\mathcal{L}_\dagger + J_z\mathcal{L}_z)[\hat{x}\hat{x} + \hat{y}\hat{y}]\mathcal{L}_y^T] \tag{B34}$$

$$\Gamma_{aJ_z} = \frac{-8\pi NT^2}{\sigma_r^2 a^5} Tr[(J_x\mathcal{L}_x + J_y\mathcal{L}_\dagger + J_z\mathcal{L}_z)[\hat{x}\hat{x} + \hat{y}\hat{y}]\mathcal{L}_z^T] \tag{B35}$$

$$\Gamma_{eJ_x} = \Gamma_{eJ_y} = 0 \tag{B36}$$

$$\Gamma_{eJ_z} = \frac{NT}{\sigma_r^2 a} \tag{B37}$$

$$\Gamma_{\Phi_0 J_x} = \Gamma_{\Phi_0 J_y} = \Gamma_{\Phi_0 J_z} = 0 \tag{B38}$$

$$\Gamma_{\Theta_x J_x} = \frac{NT}{2\pi\sigma_r^2 a} Tr[\mathcal{L}_x[A_1\hat{x}\hat{x} + (A_2 - A_1)\hat{y}\hat{y}]\mathcal{L}_x^T] \tag{B39}$$

$$\Gamma_{\Theta_y J_y} = \frac{NT}{2\pi\sigma_r^2 a} Tr[\mathcal{L}_y[A_1\hat{x}\hat{x} + (A_2 - A_1)\hat{y}\hat{y}]\mathcal{L}_y^T] \tag{B40}$$

$$\Gamma_{\Theta_z J_z} = \frac{-NT}{2\pi\sigma_r^2 a} Tr[\mathcal{L}_z[A_1\hat{x}\hat{x} + (A_2 - A_1)\hat{y}\hat{y}]\mathcal{L}_z^T]. \tag{B41}$$

Appendix C: Likelihood and MCMC

1. Bayesian formalism

To separate issues pertaining to measurement from physics from dynamics, we describe results using three measurement scenarios: (a) an idealized measurement model, where the position or velocity of each star can be measured at known times, as if via an array of local observers surrounding the black hole; (b) a plausible model, where only the radial velocity and transverse angle can be measured, on known null rays; and (c) a model for pulsar timing.

Specifically, our first measurement model assumes each star's position $\vec{r}_\alpha$ is measured to be $\vec{x}_{\alpha,k}$ on times t_k with measurement error σ_r. We will henceforth use Greek subscripts α to index stars *or* parameters; small roman subscripts like k to index measurements; and large roman symbols to denote vector components. Since local measurements are performed, the distance to the black hole (and astrometry) do not enter into the analysis. For this model, the probability distribution of the data is

$$p(D|\lambda) = (2\pi\sigma_r^2)^{-3N/2} \exp - \sum_{\alpha,k} \frac{(\vec{r}_\alpha(t_k|\lambda) - \vec{x}_k)^2}{2\sigma_r^2}. \tag{C1}$$

Because of its simplicity, we will use this analytically trivial model when illustrating how physics break the degeneracy.

A more realistic measurement model accounts for the unknown distance to the Galactic Center; the unknown mass of the Galactic Center black hole; and the fact that only projected sky positions $\vec{\theta}_k$ and radial velocities $v_{r,k}$ can be measured. For this model, the probability distribution of the data are

$$\begin{aligned} p(D|\lambda) = (2\pi\sigma_\theta^2)^{-2N/2} \exp - \sum_{\alpha,k} \frac{(P_\perp \vec{r}_\alpha(t_k|\lambda) - \vec{\theta}_k R)^2}{2\sigma_\theta^2} \\ \times (2\pi\sigma_v^2)^{-N/2} \exp - \sum_{\alpha,k} \frac{(\hat{N}\cdot\partial_t \vec{r}_\alpha(t_k|\lambda) - v_N)^2}{2\sigma_v^2}, \end{aligned} \tag{C2}$$

combined with a prior for R, the distance to the Galactic Center. A more realistic model still accounts for light propagation time across the stellar orbit [60]; light bending near the black hole note we are in harmonic coordinates; higher order terms in the doppler equation [16, 17]

Finally, the orbit of a pulsar around a black hole can be reconstructed by timing. Pulsar timing corresponds to fitting a model to pulse arrival times, to insure they arrive in regular intervals in the source frame. Roughly speaking, the model corresponds to fitting the proper time of the pulsar's orbit, which can be measured to some accuracy.

2. Fisher matrix

To illustrate the mechanics of a Fisher matrix calculation, we employ the idealized measurement model of Eq. (C1) in the special case that the observed data is exactly as predicted by some set of model parameters λ' [i.e., $\vec{x}_k = \vec{r}(t_k|\lambda')$]. Using a first-order Taylor series expansion $\vec{r}(t_k|\lambda) - \vec{r}(t_k|\lambda') \simeq \delta\lambda^b \partial\vec{r}/\partial\lambda_b$ for the position versus parameters λ, we find the conditional probability of the data given λ can be approximated by

$$\ln p(D|\lambda) = \text{const} - \frac{1}{2}\Gamma_{ab}\delta\lambda_a\delta\lambda_b \tag{C3}$$

$$\Gamma_{ab} = \sum_{\alpha,k} \frac{1}{\sigma_r^2}\frac{\partial\vec{r}_\alpha}{\partial\lambda_a}\frac{\partial\vec{r}_\alpha}{\partial\lambda_b}. \tag{C4}$$

This expression applies in general, no matter how the solution $r(t)$ is solved or approximated. By using an approximate analytic solution, the orbit-averaged secular solution in Eq. (11), we can estimate the accuracy to which parameters can be measured using a simple orbit average over a Newtonian solution. For example, for parameters λ which do not appear in the unperturbed Newtonian solution, like the black hole spin J or external potential, the Fisher matrix takes the form

$$\Gamma_{ab} = \sum_k \frac{t_k^2}{\sigma_r^2}\frac{\partial\Omega^A}{\partial\lambda_a}\frac{\partial\Omega^B}{\partial\lambda_b}(-i\mathcal{L}_A\vec{r}_o(t_k))^C(-i\mathcal{L}_B\vec{r}_o(t_k))^C. \tag{C5}$$

In fact, as a first approximation, these components of Fisher matrix can be approximated using the orbit's moment of inertia $I_{ab,N} = \langle r_{o,a}r_{o,b}\rangle$:

$$\Gamma_{ab} \simeq \tfrac{t^3}{3N}\tfrac{\partial\Omega^A}{\partial\lambda_a}\tfrac{\partial\Omega^B}{\partial\lambda_b}\text{Tr}[(-i\mathcal{L}_A)I(-i\mathcal{L}_B)^T]. \tag{C6}$$

Having estimated the Fisher matrix and hence approximated $p(\{d\}|\lambda)$ by a Gaussian, we can further construct marginalized distributions for λ_A in $\lambda = (\lambda_A, \lambda_a)$ by integrating out the variables λ_a.

3. Toy model: tests in $\vec{r}$ using MCMC

We show that MCMC agree with both the numerical and the analytic Fisher matrices via toy models: As a concrete example, in the Cartesian coordinates with its origin at the black hole center and $\{x_i, y_i, z_i\}$ as the observables, we model a Newtonian circular orbit with parameters $\{a, \Phi_0, \beta, \gamma, \psi\}$ and measure its semimajor axis or radius in two cases shown in the top panel of Figure 8, as well as an elliptical orbit with parameters $\{a, e, \Phi_0, \beta, \gamma, \psi, J_x, J_y, J_z\}$ and measure its spin magnitude in two cases shown in the bottom panel of Figure 8. For the measurement of the radius (denoted with symbol a as it is semimajor axis with $e = 0$) of a circular orbit, the two cases are treating only the semimajor axis as uncertain as shown in the black solid line and treating all orbital parameters as uncertain as shown in the blue solid line. The dashed lines show the measurement uncertainty from the Fisher matrix method where both the numerical Fisher matrix in Eq. (C4) and the analytic Fisher matrix component for the radius in Eq. (B12) give the same value, with $a = 2800M, N = 700, \sigma_r = 1.0M, T = 100\ weeks, \Delta t = 1\ day$. Comparing the corresponding solid and the dashed lines for the two cases respectively, we can see that MCMC agree well with Fisher matrix for the measurement uncertainties in the radius of the orbits. Similar conclusion can be drawn for the measurement of the magnitude of black spin. Note that the numerical Fisher matrix in Eq. (C4) and the analytic Fisher matrix in Eq. (B32) are used and they are also the same. They are evaluated using the same initial parameters as the top panel, except that $\sigma_r = 0.1M$ and $e = 0.01$ and evolved according to Eq. (1).

[1] D. Psaltis and T. Johannsen, Journal of Physics Conference Series **283**, 012030 (2011), arXiv:1012.1602 [astro-ph.HE].
[2] T. Do *et al.*, **51**, 530 (2019), arXiv:1903.05293 [astro-ph.GA].

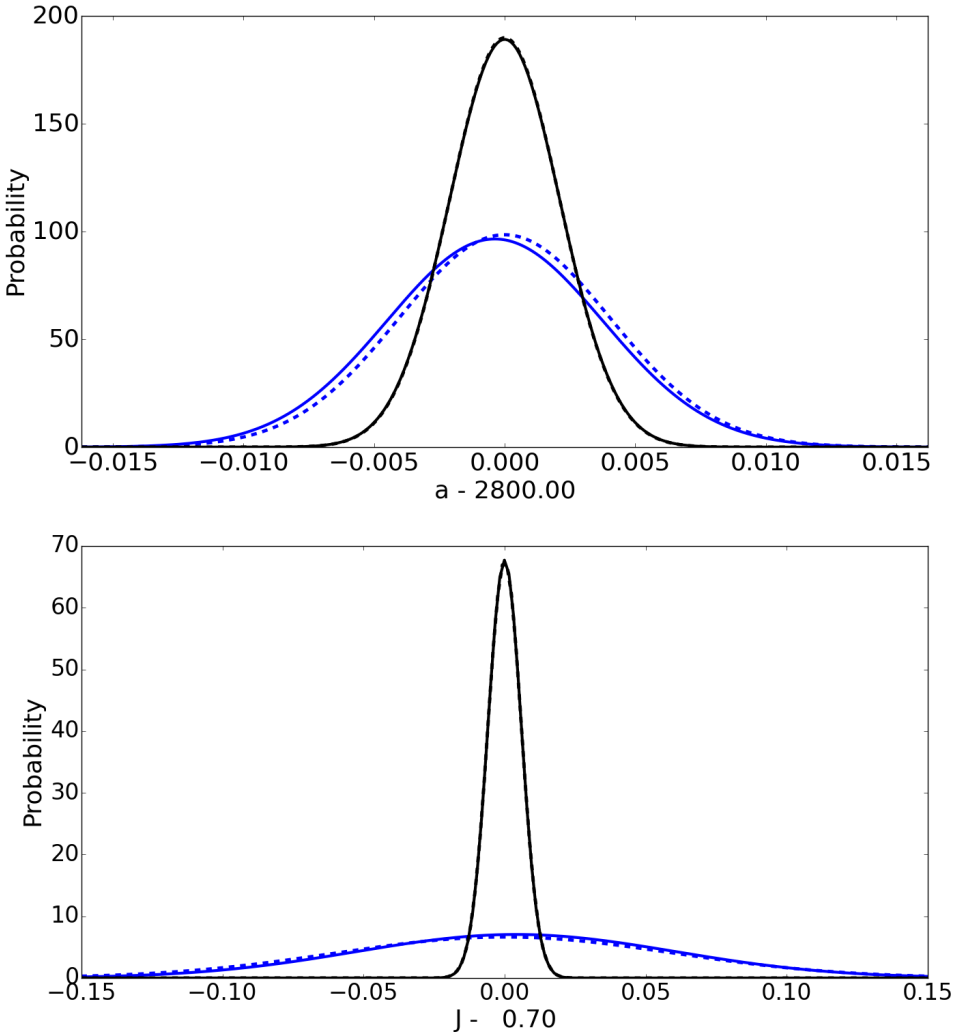

FIG. 8. **Measuring properties of an orbit and a BH for idealized measurement model.** *Top panel*: Demonstration of how accurately the radius of a Newtonian circular orbits can be measured by our MCMC code, assuming the only unknown parameter is the orbital radius (black) and assuming no parameters are known (blue). For comparison, the dotted curves show the results from our Fisher matrix calculations. *Bottom panel*: Demonstration of how accurately the black hole spin J can be measured, assuming the only unknown parameter is the black hole spin magnitude $\chi = J/M^2$ (black) and assuming both the orbit and black hole spin vector are unknown (blue). The dotted curves show the result from Fisher matrix calculations.

[3] H. Falcke, F. Melia, and E. Agol, The Astrophysical Journal Letters **528**, L13 (2000), astro-ph/9912263.
[4] K. Akiyama *et al.* (Event Horizon Telescope), Astrophys. J. **875**, L1 (2019), arXiv:1906.11238 [astro-ph.GA].
[5] D. Psaltis, Gen. Rel. Grav. **51**, 137 (2019), arXiv:1806.09740 [astro-ph.HE].
[6] C. S. Reynolds, Nature Astron. **3**, 41 (2019), arXiv:1903.11704 [astro-ph.HE].
[7] V. I. Dokuchaev, N. O. Nazarova, and V. P. Smirnov, Gen. Rel. Grav. **51**, 81 (2019), arXiv:1903.09594 [astro-ph.HE].
[8] M. Daniel, K. Moriyama, V. Fish, and K. Akiyama, in *American Astronomical Society Meeting Abstracts #235*, American Astronomical Society Meeting Abstracts, Vol. 235 (2020) p. 369.15.
[9] D. Psaltis *et al.* (Event Horizon Telescope), Phys. Rev. Lett. **125**, 141104 (2020), arXiv:2010.01055 [gr-qc].
[10] A. E. Broderick, A. Loeb, and M. J. Reid, Astrophys. J. **735**, 57 (2011), arXiv:1104.3146 [astro-ph.HE].
[11] A. M. Ghez, S. Salim, S. D. Hornstein, A. Tanner, J. R. Lu, M. Morris, E. E. Becklin, and G. Duchêne, Astrophys. J. **620**, 744 (2005), arXiv:astro-ph/0306130 [astro-ph].
[12] A. M. Ghez, S. Salim, N. N. Weinberg, J. R. Lu, T. Do, J. K. Dunn, K. Matthews, M. R. Morris, S. Yelda, E. E. Becklin, T. Kremenek, M. Milosavljevic, and J. Naiman, Astrophys. J. **689**, 1044 (2008), arXiv:0808.2870.
[13] S. Gillessen, F. Eisenhauer, S. Trippe, T. Alexander, R. Genzel, F. Martins, and T. Ott, Astrophys. J. **692**, 1075 (2009), arXiv:0810.4674.

[14] L. Meyer, A. M. Ghez, R. Schödel, S. Yelda, A. Boehle, J. R. Lu, T. Do, M. R. Morris, E. E. Becklin, and K. Matthews, Science **338**, 84 (2012), arXiv:1210.1294 [astro-ph.GA].
[15] S. Gillessen, P. M. Plewa, F. Eisenhauer, R. Sari, I. Waisberg, M. Habibi, O. Pfuhl, E. George, J. Dexter, S. von Fellenberg, T. Ott, and R. Genzel, Astrophys. J. **837**, 30 (2017), arXiv:1611.09144 [astro-ph.GA].
[16] S. Zucker, T. Alexander, S. Gillessen, F. Eisenhauer, and R. Genzel, The Astrophysical Journal Letters **639**, L21 (2006), astro-ph/0509105.
[17] S. Zucker and T. Alexander, The Astrophysical Journal Letters **654**, L83 (2007), astro-ph/0609753.
[18] S. Naoz, C. M. Will, E. Ramirez-Ruiz, A. Hees, A. M. Ghez, and T. Do, The Astrophysical Journal Letters **888**, L8 (2020), arXiv:1912.04910 [astro-ph.GA].
[19] N. N. Weinberg, M. Milosavljević, and A. M. Ghez, Astrophys. J. **622**, 878 (2005), arXiv:astro-ph/0404407.
[20] C. M. Will, The Astrophysical Journal Letters **674**, L25 (2008), arXiv:0711.1677.
[21] D. Merritt, T. Alexander, S. Mikkola, and C. M. Will, Phys. Rev. D **81**, 062002 (2010), arXiv:0911.4718 [astro-ph.GA].
[22] C. M. Will and M. Maitra, Phys. Rev. D **95**, 1 (2017), arXiv:1611.06931.
[23] R. Abuter *et al.* (GRAVITY), Astron. Astrophys. **636**, L5 (2020), arXiv:2004.07187 [astro-ph.GA].
[24] G. Fragione and A. Loeb, Astrophys. J. **901**, L32 (2020), arXiv:2008.11734 [astro-ph.GA].
[25] K. Liu, N. Wex, M. Kramer, J. M. Cordes, and T. J. W. Lazio, Astrophys. J. **747**, 1 (2012), arXiv:1112.2151 [astro-ph.HE].
[26] N. Rea, P. Esposito, J. A. Pons, R. Turolla, D. F. Torres, G. L. Israel, A. Possenti, M. Burgay, D. Vigano', R. Perna, L. Stella, G. Ponti, F. Baganoff, D. Haggard, A. Papitto, A. Camero-Arranz, S. Zane, A. Minter, S. Mereghetti, A. Tiengo, R. Schoedel, M. Feroci, R. Mignani, and D. Gotz, (2013), arXiv:1307.6331 [astro-ph.GA].
[27] N. Wex, K. Liu, R. P. Eatough, M. Kramer, J. M. Cordes, and T. J. W. Lazio, in *IAU Symposium*, IAU Symposium, Vol. 291 (2013) pp. 171–176, arXiv:1210.7518 [gr-qc].
[28] R. S. Wharton, S. Chatterjee, J. M. Cordes, J. S. Deneva, and T. J. W. Lazio, Astrophys. J. **753**, 108 (2012), arXiv:1111.4216 [astro-ph.HE].
[29] D. Psaltis, N. Wex, and M. Kramer, Astrophys. J. **818**, 121 (2016), arXiv:1510.00394 [astro-ph.HE].
[30] N. Rea, P. Esposito, J. A. Pons, R. Turolla, D. F. Torres, G. L. Israel, A. Possenti, M. Burgay, D. Viganò, A. Papitto, R. Perna, L. Stella, G. Ponti, F. K. Baganoff, D. Haggard, A. Camero-Arranz, S. Zane, A. Minter, S. Mereghetti, A. Tiengo, R. Schödel, M. Feroci, R. Mignani, and D. Götz, The Astrophysical Journal Letters **775**, L34 (2013), arXiv:1307.6331 [astro-ph.GA].
[31] J. R. Lu, T. Do, A. M. Ghez, M. R. Morris, S. Yelda, and K. Matthews, Astrophys. J. **764**, 155 (2013), arXiv:1301.0540 [astro-ph.SR].
[32] F. Peißker, A. Eckart, M. Zajaček, B. Ali, and M. Parsa, Astrophys. J. **899**, 50 (2020), arXiv:2008.04764 [astro-ph.GA].
[33] L. Iorio, arXiv e-prints , arXiv:2009.01158 (2020), arXiv:2009.01158 [gr-qc].
[34] M. L. Graham *et al.*, (2019), arXiv:1904.05957 [astro-ph.HE].
[35] A. Hees, T. Do, A. M. Ghez, G. D. Martinez, S. Naoz, E. E. Becklin, A. Boehle, S. Chappell, D. Chu, A. Dehghanfar, K. Kosmo, J. R. Lu, K. Matthews, M. R. Morris, S. Sakai, R. Schödel, and G. Witzel, Phys. Rev. Lett. **118**, 211101 (2017), arXiv:1705.07902 [astro-ph.GA].
[36] S. Jia, J. R. Lu, S. Sakai, A. K. Gautam, T. Do, J. Hosek, M. W., M. Service, A. M. Ghez, E. Gallego-Cano, R. Schödel, A. Hees, M. R. Morris, E. Becklin, and K. Matthews, Astrophys. J. **873**, 9 (2019), arXiv:1902.02491 [astro-ph.GA].
[37] T. Do *et al.*, Science **365**, 664 (2019), arXiv:1907.10731 [astro-ph.GA].
[38] D. Merritt, *Dynamics and Evolution of Galactic Nuclei* (Princeton University Press, 2013).
[39] C. Will, *Theory and Experiment in Gravitational Physics* (Cambridge University Press, 1985).
[40] W. Tichy and E. Flanagan, Phys. Rev. D **84** (2011), arXiv:1101.0588 [gr-qc].
[41] L. Sadeghian and C. M. Will, Classical and Quantum Gravity **28**, 225029 (2011), arXiv:1106.5056 [gr-qc].
[42] L. Iorio, Phys. Rev. D **84**, 124001 (2011), arXiv:1107.2916 [gr-qc].
[43] A. Goodman, `https://www.cfa.harvard.edu/~agoodman/ISO/plan98/galctr.html` (1998).
[44] M. A. Requena-Torres, J. Martín-Pintado, A. Rodríguez-Franco, S. Martín, N. J. Rodríguez-Fernández, and P. de Vicente, (2006), 10.1051/0004-6361:20065190, astro-ph/0605031v2.
[45] J. Goodman and J. Weare, Commun. Appl. Math. Comput. Sci. **5**, 65 (2010).
[46] D. Foreman-Mackey, D. W. Hogg, D. Lang, and J. Goodman, PASP **125**, 306 (2013), 1202.3665.
[47] S. Gillessen *et al.*, Proc. SPIE Int. Soc. Opt. Eng. **7734**, 77340Y (2010), arXiv:1007.1612 [astro-ph.IM].
[48] GRAVITY Collaboration, Astronomy & Astronphysics **602** (2017), 10.1051/0004-6361/201730838, arXiv:0711.1677.
[49] M. Freitag, P. Amaro-Seoane, and V. Kalogera, Astrophys. J. **649**, 91 (2006), astro-ph/0603280.
[50] M. Preto and P. Amaro-Seoane, The Astrophysical Journal Letters **708**, L42 (2010), arXiv:0910.3206 [astro-ph.GA].
[51] T. Alexander and C. Hopman, Astrophys. J. **697**, 1861 (2009), arXiv:0808.3150.
[52] D. Merritt, Astrophys. J. **718**, 739 (2010), arXiv:0909.1318 [astro-ph.GA].
[53] R. Genzel, F. Eisenhauer, and S. Gillessen, Reviews of Modern Physics **82**, 3121 (2010), arXiv:1006.0064 [astro-ph.GA].
[54] T. Alexander and O. Pfuhl, Astrophys. J. **780**, 148 (2014), arXiv:1308.6638 [astro-ph.GA].
[55] I. Bartos, Z. Haiman, B. Kocsis, and S. Márka, Physical Review Letters **110**, 221102 (2013), arXiv:1302.3220 [astro-ph.GA].
[56] T. A. Apostolatos, C. Cutler, G. J. Sussman, and K. S. Thorne, Phys. Rev. D **49**, 6274 (1994).
[57] L. Blanchet, (arXiv:1310.1528) (2013).
[58] A. Buonanno, Y. Chen, and T. Damour, Phys. Rev. D **74**, 104005 (2006), gr-qc/0508067.
[59] Han, W.-B, Research in Astronomy and Astronphysics **14** (2014), 10.1088/1674-4527/14/11/005, arXiv:1404.5160.
[60] F. Zhang, Y. Lu, and Q. Yu, Astrophys. J. **809**, 127 (2015), arXiv:1508.06293.